Stochastic receptivity of laminar compressible boundary layers: an input-output analysis

Frédéric Alizard, Tobias Gibis, Björn Selent, Ulrich Rist, Christoph Wenzel

Stochastic receptivity of laminar compressible boundary layers: an input-output analysis.

Frédéric Alizard,[1] Tobias Gibis,[2] Björn Selent,[2] Ulrich Rist,[2] and Christoph Wenzel[2]

[1] *Laboratoire de mécanique des fluides et d'acoustique, Claude Bernard University Lyon 1, Villeurbanne, France*

[2] *Institute of Aerodynamics and Gas Dynamics, University of Stuttgart, 70569 Stuttgart, Germany*

(Dated: June 30, 2022)

This study extends the input-output framework for the receptivity analysis of an incompressible boundary layer introduced by Ran *et al.* (*Stochastic receptivity analysis of boundary layer flow* Phys. Rev. Fluids. **4**, 093901, 2019) to the laminar adiabatic supersonic case. Spatially distributed in the wall-normal direction, a delta-correlated Gaussian noise is considered as input, both including the velocity and temperature fields. Similarly, components of the resulting velocity and/or temperature fields are chosen as outputs. To study effects on the boundary layer the measurements of the output are restricted within the δ_{99} boundary layer thickness implying, however, that effects like acoustic radiation to the freestream are outside the scope of the present analysis. The main goal of the study is twofold: First, to demonstrate the potential of the chosen approach by comparison with familiar results; second, to extend the current state of knowledge in the compressible regime in selected points by exploiting the extended capabilities of the chosen framework. To this end, the importance of the different inputs – especially the temperature effects – for the amplification of two-dimensional, oblique flow structures and streaks are discussed. Furthermore, the influence of first and second Mach modes (not present in the incompressible regime) is identified within the stochastic framework for the first time and results are discussed in the light of previous receptivity analyses where the output is restricted to a single mode. By varying the spatial distribution of the forcing, the dependence of the receptivity on the wall-normal position, where the forcing is introduced, is illustrated and discussed.

Finally, dominant coherent structures are identified by evaluating the first singular vector of the correlation matrix (POD modes). By analyzing the dependence of both forcing and response POD modes on the choice of the measured component, further insight is provided about the contribution of temperature fluctuation to the stochastically maintained variance of the system.

1. INTRODUCTION

The prediction of the laminar-turbulent transition of compressible boundary layers is of great interest for improving the performance of supersonic aircraft. Indeed, the laminar-turbulent transition of the boundary layer has a strong impact on drag, aerodynamic heating and mechanical fatigue of the body. Successful prediction of the transition point, however, requires an accurate understanding of the complex mechanisms that drive the flow to turbulence, and thus represents a key element in the design of control strategies to delay transition[1].

In principal, the laminar-turbulent transition path divides into three stages: the receptivity, the linear growth of instability modes and secondary mechanisms. The receptivity step consists in converting various environmental disturbances into boundary layer instability modes[2]. The linear growth is amplified either through an exponential mode[3] or due to non-modal effects[4]. During the last stage, the growth of perturbations is very fast and the breakdown to turbulence occurs.

Assuming a weak ambient turbulence intensity and/or a controlled transition, the linear growth is associated with the most unstable wave, whereas the latter can be obtained by solving the eigenvalue problem derived from the linear stability theory. For the low Mach number case, the unstable boundary layer eigenmode is the so-called two-dimensional Tollmien-Schlichting (TS) wave, for supersonic boundary layers, Mack[5] found evidence for the existence of multiple inviscid acoustic modes when the relative Mach number (*i.e.* the local Mach number of the base flow in a frame parallel to the wave vector) is greater than 1. Among them, Mack[5] have shown that the least stable of these additional modes, also called the second mode, becomes unstable at Mach numbers larger than 4 for an adiabatic wall. In particular, that for two-dimensional disturbances, the second mode is the most amplified mode for $M_\infty > 4$ and that the most amplified Tollmien-Schlichting wave (referenced as the first mode) is oblique rather than two-dimensional. Arnal[6] and Özgen & Kirkali[7] extended Mack's results to a wide range of Mach numbers and various fluid properties (such as the reference temperature for instance). The authors showed that the oblique wave direction of the most unstable mode is almost unaffected for freestream Mach number greater than 4 (typically around 60^o). More recently, the effect of wall cooling onto linear stability of a supersonic boundary layer has been investigated by Bitter & Shepherd[8] .

As the external disturbance amplitude increases, the second step of transition is mainly driven by non-modal mechanisms. An appropriate superposition of eigenmodes may experience a transient energy growth due to the non-orthogonality of the eigenvectors. Laminar-turbulent transition in the boundary layer flows is then dominated by streamwise elongated streaks and the breakdown

is caused by their sinuous/varicose secondary instabilities. The physical mechanism behind the emergence of streaks is the so-called lift-up effect[9]. The growth results from the tilting of streamwise vorticity onto wall-normal vorticity under the action of the basic shear. This mechanism occurs in both subsonic and supersonic regimes even if characteristic temporal and spatial scales depend on the Mach number (see Hanifi *et al.*[10], Zuccher *et al.*[11], Tumin & Reshotko[12] and Tempelmann *et al.*[13] for theoretical analyses within either a temporal or a spatial framework, respectively).

As mentioned above, the receptivity analysis aims to assess the effectiveness with which external sources excite flow structures. In this vein, Hill[14] introduced a linear theoretical framework for an incompressible boundary layer flow using the solution of the adjoint Orr-Sommerfeld operator, aiming to indicate the forcing (components and wall-normal positions) which would induce the largest response of the TS mode. It comes out that the receptivity crucially depends on the non-normality of the underlying dynamical operator and that several damped modes may contribute to the asymptotic response of the TS wave.

By using direct numerical simulations (DNS), the receptivity of the adiabatic supersonic boundary layer to various forcing disturbances has been addressed by Malik et *al.*[15] and Ma & Zhong[16]. Especially, Ma & Zhong[16] have found that – in addition to the first and second modes – also a family of stable distinct modes (named modes I, II, and so on by the authors) exists besides the already known which play a significant role in the excitation of the unstable Mack modes; these modes do not have any counterpart in the incompressible regime. Following the same methodology as in the prior investigation of Ma & Zhong[16], Wang & Zhong[17] studied the receptivity of a flat plate boundary layer at $M_\infty = 5.92$ to periodic two-dimensional wall excitations. It was shown that instability waves generated by wall-normal blowing and suction at the wall reach higher amplitudes than those excited by either streamwise velocity or temperature disturbances. These observations are consistent with the analytical results given by Fedorov & Khokhlov[18].

More recently, Tumin *et al.*[19] extended the linear incompressible receptivity theory of Hill[14] to the compressible problem. The receptivity of the first and second modes is then analyzed in detail either with the help of the linear receptivity model or by exploiting DNS data using a multimode decomposition technique for a biorthogonal system[20]. A good comparison is observed between the theoretical receptivity coefficient distribution and the amplitude filtered output from the DNS computation through a projection onto the different modes. It clearly confirms the necessity of using a multimode framework to evaluate the receptivity mechanisms of the first and second modes and further supports the statement established by Ma & Zhong[16] (see also Fedorov[21] for a review).

Although the aforementioned studies have greatly improved the understanding of compressible

receptivity, two main gaps can be identified. Firstly, some essential questions like the receptivity of streaks, for instance, have not yet been sufficiently discussed; the emergence of these elongated structures may compete with the excitation of the first and second modes in certain situations. Secondly, all of the studies listed are merely restricted to a forcing that only includes a single frequency which does not properly reflect broadband external excitation (free-stream turbulence and surface roughness for instance). For incompressible flows, it has been shown by e.g. Farrell & Ioannou[22] and Bamieh & Dahleh[23] that the level of the variance of the linear response can be slightly enhanced due to the non-normality of the governing operator for various linearly stable canonical shear flows. The amplification of stochastic excitation is then a consequence of an optimal superposition of eigenmodes and has close mathematical connections with non-normal growth[24]. Besides, Hwang & Cossu[25] have shown that the characteristic spanwise scale of streaks is different whether the harmonic or the white noise forcing is considered for the incompressible turbulent Couette flow. It indicates that the two approaches are complementary to understand which most representative scale may emerge due a stochastic forcing and what is its spectral content. Solely restricted to the incompressible case, these questions inspired a stochastic receptivity theory based on an input/output framework by Ran *et al.*[26], which has been used to study the influence of the forcing (both wall-normal positions and spatial correlations properties) onto the excitation of streaks and TS waves. For that purpose, the authors have introduced a receptivity coefficient as the ratio of the measurement of the variance of the response (*i.e.* the output) to the variance associated with the forcing (*i.e.* the input). Furthermore, the estimation of the power cross-spectral density tensor using the resolvent operator is explicitly given by the authors, extending the standard resolvent analysis[27] to stochastically forced flows (see also Morra *et al.*[28] for further details).

Concluding from the studies introduced, it is evident that a lot of work dealing with the receptivity of shear flows in the context of an input/output strategy has been done so far, but mainly with a strict focus on incompressible flows. The few recent analyses that deal with compressible flows are concerned with computing the linear response to harmonic forcing. For instance, Dwidedi *et al.*[29] quantified the amplification of streaks due to external harmonic excitation in supersonic laminar boundary layer and hypersonic compression ramp flows. Using the same framework, Dwidedi *et al.*[30] investigated oblique transition in a Mach 5 hypersonic flow over an adiabatic slender double-wedge. For the turbulent regime, Bae *et al.*[31] and Dawson & McKeon[32] employed a resolvent analysis to identify the amplification of coherent structures in supersonic turbulent boundary layers and extend the prior study focusing on linear transient growth carried out by

Alizard *et al.*[33]. Very recently, Madhusudanan & McKeon[34] investigated the stochastic response of the laminar supersonic boundary layer. They mainly focused on the amplification of streaks for several Mach numbers and wall temperatures. In particular, they have shown that streaks are not amplified by an input restricted to either the temperature or density disturbances.

Although the above findings provide a good understanding of the amplification of first and second modes and streaks in supersonic boundary layers, it should be pointed out that the above mentioned models have some limitations. Firstly, in contrast to the incompressible case, the previous receptivity analyses are mainly restricted to external harmonic excitations. While it provides strong informations about the sensitivity to forcing frequencies, they may not fully capture natural sources of excitation and thus miss the cumulative effect of the different frequencies onto characteristic spatial scales. Secondly, the specific role of the temperature disturbance for the receptivity process of the first and second modes (active or passive effects) has not yet been fully addressed which is known, however, to be of great relevance in certain scenarios (see Fedorov & Tumin[35] for instance). Thirdly, the crucial influence of the wall-normal position where the forcing is imposed on the amplification of the various flow structures[26] has not been systematically studied for a wide range of streamwise and spanwise scales in the compressible case. This specific point is of major interest in laminar-turbulent transition controlled by localized disturbances. For instance, plasma actuators are widely used in supersonic boundary layers to prevent flow separation. In that case, the effectiveness of such actuators could be further improved in optimizing the orientation, wall-normal position and spanwise distribution of the induced jets within the boundary layer.

1.1. Objectives of this study

Motivated by these questions, it is the objective of the present work to revisit the linear receptivity of supersonic boundary layers with a hope to address the inherent limitations mentioned above. Motivated by the success in incompressible investigations, the ideal tool to achieve this goal appears to be the stochastic input/output receptivity framework introduced by Ran *et al.*[26]. On the one hand, this will allow to both study the effects of the various inputs (including components and/or spatial localizations) into the excitation of characteristic scales that coincide with streaks, first and second modes. On the other hand, it allows to overcome the inherent difficulties associated with a modal framework as none specific mode is promoted for the output due to the stochastic approach. Thus, the present framework provides a more general tool to investigate the receptivity process associated with the amplification of different spatial scales.

The paper is organized as follows. We first introduce the receptivity model in section 2. Section 3 is devoted to characterize the evolution of the receptivity coefficient with the Mach number and various inputs. Results will be examined through the spectral content associated with the measurement. Using response and forcing proper orthogonal decompositions (POD), the dominant flow structures associated with the different peaks in the receptivity coefficient will then be investigated to draw a complete picture between inputs and outputs. Finally, the conclusions are summarized in section 4 and prospects are given.

2. INPUT/OUTPUT FRAMEWORK FOR THE RECEPTIVITY ANALYSIS

In this section, the theoretical tool used to investigate the receptivity process associated with a supersonic boundary layer subjected to an external stochastic forcing is introduced, which thus extends the input/output framework introduced by Ran *et al.*[26] to the compressible case. Within this general framework, the output is characterized using the second-order statistics of the linear boundary layer response and the base flow is assumed to be wall-parallel, see Ran *et al.*[26] for a justification/consequences of this choice.

Formulated for a cartesian coordinate system with $(x, y, z) = (x_1, x_2, x_3)$ the streamwise, wall-normal and spanwise directions, respectively, the Navier-Stokes equations for a compressible perfect gas read:

$$\begin{aligned}
&\frac{\partial \rho}{\partial t} + \frac{\partial \rho u_j}{\partial x_j} = 0, \\
&\frac{\partial \rho u_i}{\partial t} + \frac{\partial \rho u_i u_j}{\partial x_j} = -\frac{\partial p}{\partial x_i} + \frac{\partial \sigma_{ij}}{\partial x_j}, \\
&\frac{\partial \rho C_v T}{\partial t} + \frac{\partial \rho C_v T u_j}{\partial x_j} = -\frac{\partial}{\partial x_j}\Psi_j + \sigma_{ij}\frac{\partial u_i}{\partial x_j} - p\frac{\partial u_i}{\partial x_i}
\end{aligned} \tag{1}$$

where ρ, p, u_i and T are density, pressure, the ith velocity component and temperature, respectively, and C_v the specific heat at constant volume. The viscous stress tensor σ_{ij} and the heat flux vector Ψ_j components are defined as

$$\sigma_{ij} = \mu(T)\left(\frac{\partial u_i}{\partial x_j} + \frac{\partial u_j}{\partial x_i}\right) - \frac{2}{3}\mu(T)\,\delta_{ij}\frac{\partial u_k}{\partial x_k},$$

$$\Psi ij = -\frac{C_p \mu(T)}{Pr}\frac{\partial T}{\partial x_j},$$

where δ_{ij}, Pr, C_p and $\mu(T)$ are Kronecker's delta, the Prandtl number, the specific heat at constant pressure and the molecular viscosity assuming Sutherland's law. Nondimensionalized by using their values at the freestream (referenced by the subscript ∞ hereafter), the flow is characterized by the Mach, Reynolds and Prandtl numbers:

$$M_\infty = \frac{U_\infty}{\sqrt{\gamma R T_\infty}},\ Re = \frac{\rho_\infty U_\infty l}{\mu_\infty},\ Pr = \frac{\mu_\infty Cp}{\lambda_\infty}.$$

Here, R is the specific gas constant, γ the specific heat ratio, λ the thermal conductivity, and l the length scale of the boundary-layer thickness $l = \sqrt{\mu_\infty x/(\rho_\infty U_\infty)}$ with x the dimensional coordinate measured from the leading edge, often used in studies of compressible boundary layer stability[7,10]. We restrict our analysis to the linearized dynamics around the base flow solution noted $\mathbf{Q} = (U, T)$ where U represents the mean flow velocity along x and T the temperature component of the base flow. Using the boundary layer approximation, the mean pressure is constant along the wall-normal direction and the mean density is obtained by using the perfect gas law.

2.1. Evolution model

Within the parallel flow assumption, we apply the Fourier transform in both the streamwise and spanwise direction onto the perturbation. We note the state vector $\phi(y, \mathbf{k}, t) = [u, v, w, \theta, \Pi]^T(y, \mathbf{k}, t)$ where u, v, w is the vector of the velocity fluctuations, Π, θ denote the pressure and temperature components of the perturbation and $\mathbf{k} = (\alpha, \beta)$ is the wave vector with α and β the streamwise and spanwise wavenumbers, respectively. Using the ideal gas law, the fluctuation of the density reads: $\rho' = \Pi/T - \theta/T^2$. Analogously to the incompressible regime (see Dwivedi *et al.*[36] for a recent review), an input/output framework is used for modeling the evolution model. Linearized around the basic state $\mathbf{Q}$ in the spectral space, the linear system of (1) forced by a stochastic excitation noted as $\mathbf{d}$ can thus be rewritten as:

$$\begin{aligned} \boldsymbol{\phi}_t(\mathbf{k}, t) &= \mathbf{A}(\mathbf{k}, \mathbf{Q})\,\boldsymbol{\phi}(\mathbf{k}, t) + \mathbf{B}\mathbf{d}(\mathbf{k}, t), \\ \mathbf{q} &= \mathbf{C}\boldsymbol{\phi}. \end{aligned} \tag{2}$$

Here, the operator $\mathbf{A}$ describes the linearized equations, see appendix 1, and the operator $\mathbf{B}$ determines how and in which components the stochastic excitation $\mathbf{d}$ is introduced to the linearized system. The measurement of the flow quantities is then extracted with the operator $\mathbf{C}$, generating the output $\mathbf{q}$.

Hereafter, the subscript $\mathbf{u}$, $\mathbf{v}$, $\mathbf{w}$, $\boldsymbol{\theta}$, $\boldsymbol{\Pi}$ denote the component of the input or the output vector, e.g., $\mathbf{d_u}$ is associated with the streamwise velocity component of the forcing.

2.2. Numerical formulation

To numerically solve the theoretical model introduced in (2), a spectral collocation method is used for discretization. For simplicity, all of the following considerations are to be interpreted in the context of the discretized counterpart of system (2). Hence, e.g. $\boldsymbol{\phi}$ also denotes the vector of the expansion coefficients that corresponds to values of $\boldsymbol{\phi}$ at the collocation points: $\boldsymbol{\phi} = (\boldsymbol{\phi}_0, .., \boldsymbol{\phi}_i, .., \boldsymbol{\phi}_N)$ with N the number of collocation points and $\boldsymbol{\phi_i} = (\mathbf{u}_i, \mathbf{v}_i, \mathbf{w}_i, \boldsymbol{\theta}_i, \boldsymbol{\Pi}_i)$. Similarly, the values of the density fluctuation at the collocation points are noted $\boldsymbol{\rho'}_i$.

To measure the receptivity to a given stochastic forcing, the variance of the norm of the random variable $\boldsymbol{\phi}$ has to be computed. For a physically meaningful measurement of the norm of $\boldsymbol{\phi}$ (*i.e.* the total energy for instance), we introduce a discrete inner product $\langle \cdot, \cdot \rangle_W$ such as

$$\langle \mathbf{f}_1, \mathbf{f}_2 \rangle_W = \mathbf{f}_1 \mathbf{W} \mathbf{f_2}^H,$$

where $\mathbf{f}_1$, $\mathbf{f}_2$ are two arbitrary vectors, the superscript H denotes the Hermitian transpose, and the weight matrix $\mathbf{W}$ is positive definite. The corresponding energy norm is noted $\|\mathbf{f_1}\|_W = \sqrt{\langle \mathbf{f}_1, \mathbf{f}_1 \rangle_W}$. Following the line of thought of Ran[26] to compute $\mathbb{E}\|\boldsymbol{\phi}\|_W^2$, where $\mathbb{E}$ stands for the expectation of a random variable, a coordinate transformation is employed to obtain $\|\boldsymbol{\phi}\|_W^2$ via the standard Euclidean norm (noted hereafter $\|\cdot\|$). We then introduce $\boldsymbol{\psi} = \mathbf{F}\boldsymbol{\phi}$ where $\mathbf{F}$ is determined through the Cholesky decomposition $\mathbf{W} = \mathbf{F}\mathbf{F}^H$, leading to $\boldsymbol{\psi}\boldsymbol{\psi}^H = \|\boldsymbol{\phi}\|_W^2$. Similarly, a change of variables is used for the output such as $\mathbf{g} = \mathbf{K}\mathbf{q}$, where the weight matrix for the measured quantity is noted $\mathbf{D} = \mathbf{K}\mathbf{K}^H$. Hence, expressed as a function of $\boldsymbol{\psi}$ and $\mathbf{g}$ in the new coordinate space, system (2) reads:

$$\begin{aligned} \boldsymbol{\psi}_t &= \mathbf{F}\mathbf{A}\mathbf{F}^{-1}\boldsymbol{\psi} + \mathbf{F}\mathbf{B}\mathbf{d} \\ \mathbf{g} &= \mathbf{K}\mathbf{C}\mathbf{F}^{-1}\boldsymbol{\psi}, \end{aligned} \tag{3}$$

where the energy norm for the output is easily obtained by $\mathbf{g}\mathbf{g}^H$.

Owing to the fact that variables associated with the input vector $\mathbf{d}$ can be different from those of the state vector $\boldsymbol{\phi}$, we further introduce a coordinate transformation for the forcing:

$$\overline{\mathbf{d}} = \mathbf{G}\mathbf{d},$$

where a physically meaningful norm for $\mathbf{d}$ is based on the weight matrix $\mathbf{Q} = \mathbf{G}\mathbf{G}^H$. Finally, system (3) is rewritten as

$$\begin{aligned} &\boldsymbol{\psi}_t = \overline{\mathbf{A}}\boldsymbol{\psi} + \overline{\mathbf{B}}\ \overline{\mathbf{d}} \\ &\mathbf{g} = \overline{\mathbf{C}}\boldsymbol{\psi} \\ &\text{with } \overline{\mathbf{A}} = \mathbf{F}\mathbf{A}\mathbf{F}^{-1},\ \overline{\mathbf{B}} = \mathbf{F}\mathbf{B}\mathbf{G}^{-1} \text{ and } \overline{\mathbf{C}} = \mathbf{K}\mathbf{C}\mathbf{F}^{-1}. \end{aligned} \tag{4}$$

In its reformulated form, system (4) easily allows us to assume a forcing that is δ correlated according to the standard Euclidean norm. As a consequence, the same mathematical tools that have been developed for linear stochastic systems under the assumption of a standard Euclidean norm can be utilized to solve system (4); these are briefly introduced in the next two subsections.

2.3. Receptivity coefficient

In the next, we assume that the stochastic forcing $\mathbf{d}$ is zero mean and white-in-time. We also admit that the forcing is δ correlated in the wall-normal direction with decorrelated components. Then, noting y and y' two wall-normal positions, we have:

$$\mathbb{E}\,\mathbf{d}(t,\alpha,\beta,y')\otimes\mathbf{d}(t',\alpha,\beta,y)=\mathbf{I}\delta\left(t-t'\right) \tag{5}$$

with δ the Dirac function and $\mathbf{I}$ the identity matrix; the specification of $\alpha,\ \beta$ and y is omitted for the sake of simplicity. We note $\mathbf{X}\left(t\right)$ the covariance matrix of the output:

$$\mathbf{X}\left(t\right)=\mathbb{E}\,\boldsymbol{\psi}(t)\otimes\boldsymbol{\psi}(t'). \tag{6}$$

The variance of the output $\boldsymbol{\psi}$ at time t is then equal to trace$\mathbf{X}\left(t\right)$. When the linearized dynamics associated with the system (4) is asymptotically stable (*i.e.* at a streamwise position where Re is lower than the critical Reynolds number) the infinite horizon state covariance $\mathbf{X}_\infty=\lim_{t\to\infty}\mathbf{X}\left(t\right)$ is given by the Lyapunov equation

$$\overline{\mathbf{A}}\mathbf{X}_\infty+\mathbf{X}_\infty\overline{\mathbf{A}}^H=-\overline{\mathbf{B}}\ \overline{\mathbf{B}}^H. \tag{7}$$

Note that the use of the infinite horizon state covariance and consequently equation (7) limits the framework as used in this study to the analysis of subcritical flows. The energy spectrum is noted

$$E\left(\mathbf{k}\right)=\text{trace}\left(\overline{\mathbf{C}}\mathbf{X}_\infty\overline{\mathbf{C}}^H\right).$$

The receptivity coefficient associated with $\mathbf{B}$ and $\mathbf{C}$ is then

$$C_R\left(\mathbf{k}\right)=E\left(\mathbf{k}\right) \tag{8}$$

which determines the ratio of the variance of the measured output to the variance of the external noise.

2.4. Power spectral density

To characterize the spectral content of the response, we introduce the power spectral density $R(\mathbf{k},\omega)$. By using Parseval's theorem, the energy spectrum can be expressed as

$$E(\mathbf{k}) = \frac{1}{2\pi}\int_{-\infty}^{\infty} R(\mathbf{k},\omega)\,\mathrm{d}\omega. \tag{9}$$

Here, $\boldsymbol{\mathcal{R}}(\mathbf{k},\omega)$ is the so-called resolvent operator defined as

$$R(\mathbf{k},\omega) = \mathrm{trace}\left(\boldsymbol{\mathcal{R}}(\mathbf{k},\omega)\,\boldsymbol{\mathcal{R}}(\mathbf{k},\omega)^H\right),$$

or written in terms of the new coordinates:

$$\boldsymbol{\mathcal{R}}(\mathbf{k},\omega) = \overline{\mathbf{C}}\left(\mathbf{I}i\omega - \overline{\mathbf{A}}\right)^{-1}\overline{\mathbf{B}},$$

with $i = \sqrt{-1}$.

2.5. Weight matrices

To allow for a meaningful evaluation of the physical relevance of the disturbance growth measurement, the associated norm needs to be based on a given energy. For the compressible framework, we adopt the energy norm suggested by Chu[37] and Hanifi *et al.*[10] that characterizes the total energy of the disturbance. The measurement of the total energy for the perturbation is then given by

$$\mathbf{E} = \frac{1}{2}\left(\frac{1}{\mathbf{T}}\mathbf{u}\boldsymbol{\mathcal{W}}\mathbf{u}^H + \frac{1}{\mathbf{T}}\mathbf{v}\boldsymbol{\mathcal{W}}\mathbf{v}^H + \frac{1}{\mathbf{T}}\mathbf{w}\boldsymbol{\mathcal{W}}\mathbf{w}^H + \frac{1}{\gamma(\gamma-1)\mathbf{T}^2M_\infty^2}\boldsymbol{\theta}\boldsymbol{\mathcal{W}}\boldsymbol{\theta}^H + \frac{1}{\mathbf{T}^2M_\infty^2}\boldsymbol{\rho'}\boldsymbol{\mathcal{W}}\boldsymbol{\rho'}^H\right), \tag{10}$$

where $\boldsymbol{\mathcal{W}}$ denotes the integration weights vector for the Chebyshev collocation points (see Hanifi *et al.*[10]). Note that $\mathbf{E}$ can be rewritten as

$$\mathbf{E} = \boldsymbol{\phi}\mathbf{W}\boldsymbol{\phi}^H,$$

where the weight matrix $\mathbf{W}$ is derived from (10). We recall that $\mathbf{E}$ can also be expressed using a coordinate transformation such as $\mathbf{E} = \boldsymbol{\psi}\boldsymbol{\psi}^H$. The weight matrices $\mathbf{G}$ and $\mathbf{D}$ are then built using submatrices of $\mathbf{W}$ depending on the specific choice of the input and output variables.

3. RESULTS

In this section, the input/output framework introduced is utilized to investigate the receptivity of the self-similar laminar adiabatic supersonic boundary layer. Hereby, the focus is placed on both

the role of the different inputs onto the amplification of various streamwise and spanwise scales as well as the role of its wall-normal position. All base flows were obtained by solving the self-similar compressible boundary-layer equations using a fourth-order Runge-Kutta algorithm combined with a Newton method in order to satisfy the boundary conditions. The base flows are represented on a Gauss-Lobatto grid and are obtained by interpolation with a cubic spline. The Prandtl number $Pr = 0.72$, stagnation temperature $T_0 = 333\ K$, and specific heat ratio $\gamma = 1.4$ are equal for all cases.

With an (pseudo) adiabatic no-slip condition for the fluctuations at the wall ($u, v, w, \theta = 0$) and vanishing fluctuations at the free-stream boundary ($u, w, \theta, \Pi = 0$), v and Π are discretized using polynomials of degree $N - 1$ (same boundary conditions are used in[11,20], see Vermeersch[38] for its numerical implementation). The upper boundary conditions are set to a wall-normal distance of $y_m = 600$, corresponding to between 40 and 120 boundary-layer thicknesses in the range of Mach numbers considered. The grid stretching is used as a buffer zone, so the large grid stretching rate was chosen intentionally to avoid unwanted acoustic wave reflections at artificial boundaries. For present purposes, our boundary treatment appears a robust and easy-to-use way in comparison to the effective implementation of non-reflective boundary conditions (see[39] and[40]). Hereafter, $\boldsymbol{\eta}$ denotes the vector that contains the Chebyshev collocation points $\cos(\pi \mathbf{N}/(N-1))$ where $\mathbf{N}$ includes the set of natural numbers $(0, 1, 2, ..., N-1)$. The transformation $\mathbf{y} = e(1-\boldsymbol{\eta})/(h+\boldsymbol{\eta})$ is employed to map the domain $[-1, 1]$ to the physical domain $[0, y_m]$ with $e = y_b y_m/(y_m - 2y_b)$, $h = 1 + 2e/y_m$ and for which y_b is the wall-normal location containing $(N-1)/2$ grid points (see Hanifi *et al.*[10]). For all cases, N is fixed to 401 and $y_b = 10$. Numerical codes are written in Python3 and algorithms from Scipy library are used. For the largest Mach number $M_\infty = 4.5$, the stochastic response has also been computed with $N = 601$, $y_b = 20$ and $y_m = 800$ (not shown in this manuscript for the sake of conciseness) and no significant difference has been observed.

3.1. Spectra and neutral curves

To enable an easy-to-follow discussion in the following, we shortly consider the asymptotic response of a supersonic boundary layer to forcing waves in this subsection first. For this purpose, two cases at $M_\infty = 2$ and 4.5 are considered, for which the calculated eigenmodes are characterized by a quite distinct behaviour. The $M_\infty = 2$ case is expected to show a subsonic-like behaviour, the $M_\infty = 4.5$ case is expected to be strongly influenced by e.g. the onset of the second Mack mode.

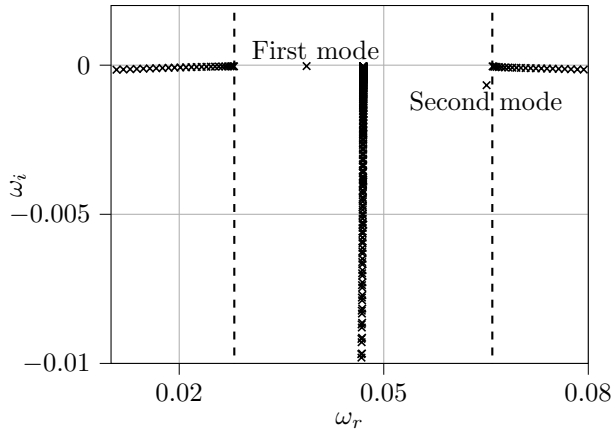

FIG. 1: $M_\infty = 4.5$ and $Re = 180$. Spectrum for $(\alpha, \beta) = (0.047, 0.071)$, compare the cross in figure 2. Slow and fast acoustic waves positions are depicted by dashed lines.

Applying a normal mode decomposition to the state vector such as:

$$\boldsymbol{\phi}(y,t) = \hat{\boldsymbol{\phi}}(y) \exp\left[i\left(\alpha x + \beta z - \omega t\right)\right],$$

with $\omega = \omega_r + i\omega_i$ the complex circular frequency, a typical spectrum for the $M_\infty = 4.5$ case is shown in figure 1 for a near-critical Reynolds number of $Re = 180$ (*i.e.* the lowest Reynolds number at which the unstable mode exists) at the close-critical wave-numbers $(\alpha, \beta) = (0.047, 0.071)$, compare the cross in figure 2. The neutral curves (i.e. curves where $\omega_i = 0$) for both the $M_\infty = 2$ and 4.5 cases are shown in figure 2. In figure 1, the spectrum exhibits two distinct modes, the first and second mode. The first mode is an extension of the incompressible TS wave, the second mode belongs to a family of trapped acoustic waves for which the boundary layer behaves as an acoustic waveguide[5,41]. Apart of these modes, two types of branch can be distinguished. The first category, the so-called continuous spectrum, is due to the freestream contribution and spans the imaginary axis where $\omega_r = \alpha$ (see Schmid & Henningson[24]). The second category is composed of slow and fast acoustic waves that propagate in the freestream. These waves are delimited by frequencies $\omega_\pm = \alpha \pm \frac{1}{M_\infty}\sqrt{\alpha^2 + \beta^2}$ that are visualised by dashed lines in figure 1. The frequency of the first mode approaches that of a slow acoustic mode as α is decreasing; the frequency of the second mode approaches that of a fast acoustic mode. The first and second modes are also referenced as slow and fast modes by Fedorov & Tumin[41].

As shown in figure 2(a) for $M_\infty = 2$, only the first mode is unstable. For $\beta = 0$, the critical Reynolds number is close to $Re_c \approx 300$ which is nearly equal to the one found in the incompressible flow regime (≈ 302), although the most unstable disturbance corresponds to an oblique wave. For the $M_\infty = 4.5$ case depicted in figure 2(b), the critical Reynolds number for the first mode is

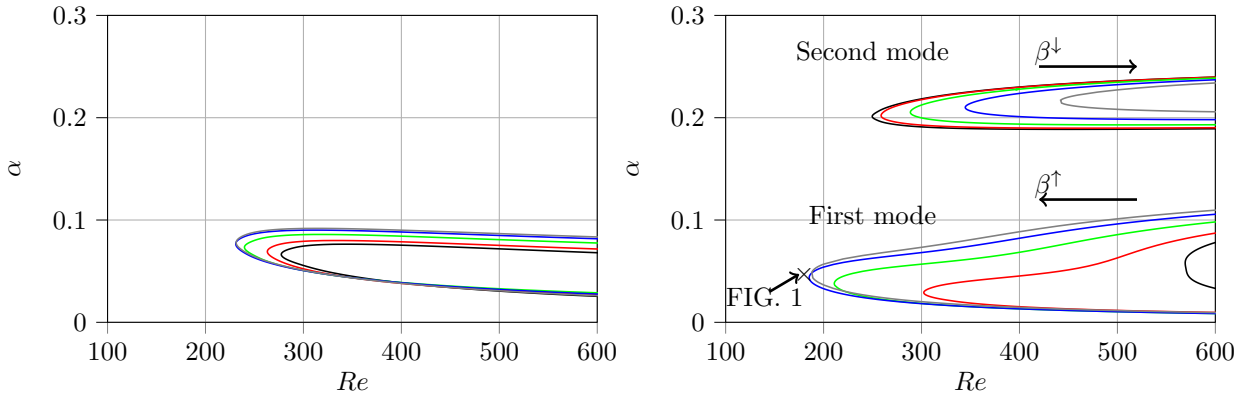

(a) $M_\infty = 2$. First mode.

(b) $M_\infty = 4.5$. First and second modes.

FIG. 2: Neutral stability curves in the plane (α, Re) for $\beta = 0,\ 0.02,\ 0.04,\ 0.06$ and 0.08 (in black, red, green, blue and gray, respectively). (a) $M_\infty = 2$ and (b) $M_\infty = 4.5$.

associated with an oblique wave with a wave-angle: $\xi = \arctan(\beta/\alpha) \approx 60^o$ ($\alpha \approx 0.047$ and $\beta \approx 0.071$). For the 2D perturbation case, the unstable region associated with the first mode moves to higher Reynolds numbers ($Re_c \approx 570$); besides the emergence of the first mode, the 2nd mode is the most amplified wave. The critical Reynolds number for the second mode is $Re_c \approx 250$ and the neutral curves for first- and second-modes are well separated for this Mach number. In summary, all results are consistent with Mack's conclusions[5] and with results given by Hanifi *et al.*[10] for the same flow case, confirming both the numerical and theoretical framework chosen. Further validation of the numerical method is given in appendix 1 including validation of the grid resolution as well as comparison with literature.

3.2. Receptivity analysis: Influence of the Mach number

3.2.1. Receptivity coefficients

Having introductively recalled the essential aspects of the various individual modes involved in the long-time dynamics in the previous section, the main goal of this section is to elaborate the influence of the Mach number on the receptivity coefficient $C_R(\alpha, \beta)$ in the multimodal framework. Due to the appearance of additional modes, all inherently included in the chosen modal spectrum, strong differences in C_R should be observed in comparison to the incompressible flow case[26] when increasing the Mach number up to 4.5. In this respect, new insights into the amplification of specific characteristic spatial scales are expected.

Both to validate the numerical method and to provide a reliable reference case for further discussion, the receptivity factor C_R is first calculated for nearly incompressible low Mach number case at $M_\infty = 0.3$ allowing a comparison with the incompressible results by Ran[26]. To allow for a meaningful comparison, the wall-normal distribution at which the forcing is applied has been defined accordingly to Ran[26] with a blending vector $\mathbf{f}$ defined as

$$\mathbf{f} = \frac{1}{\pi}\left[\arctan\left(a\left(\mathbf{y} - y_1\right)\right) - \arctan\left(a\left(\mathbf{y} - y_2\right)\right)\right]. \tag{11}$$

Consistently with Ran[26], $a = 1$, $y_1 = 0$ and $y_2 = 5$ (*i.e.* $y_2 \approx \delta_{99}$), implying that the forcing is mainly localized within δ_{99} boundary layer thickness. For comparison purposes with the incompressible case, the input fields $\mathbf{d}$ components only include the velocity field

$$\mathbf{d} = \begin{bmatrix} \mathbf{d_u} \\ \mathbf{d_v} \\ \mathbf{d_w} \\ \mathbf{d}_\theta \\ \mathbf{d_\Pi} \end{bmatrix} \text{ and } \mathbf{B} = \begin{bmatrix} \mathbf{I} & \mathbf{0} & \mathbf{0} & \mathbf{0} & \mathbf{0} \\ \mathbf{0} & \mathbf{I} & \mathbf{0} & \mathbf{0} & \mathbf{0} \\ \mathbf{0} & \mathbf{0} & \mathbf{I} & \mathbf{0} & \mathbf{0} \\ \mathbf{0} & \mathbf{0} & \mathbf{0} & \mathbf{0} & \mathbf{0} \\ \mathbf{0} & \mathbf{0} & \mathbf{0} & \mathbf{0} & \mathbf{0} \end{bmatrix} \mathbf{f}.$$

Similarly, the output $\mathbf{q}$ is extracted within the δ_{99} boundary layer thickness with a top-hat filter function $\mathbf{h}$ according to $\mathbf{q} = [\mathbf{q_u}, \mathbf{q_v}, \mathbf{q_w}, \mathbf{q}_\theta, \mathbf{q_\Pi}]^T$ and $\mathbf{C} = \mathbf{I}\mathbf{h}$. The reasons of this choice for $\mathbf{C}$ are based on two considerations: first it allows an objective comparison with results provided by Ran *et al.*[26] for the incompressible regime, secondly, it removes the acoustic signature in the freestream of the vortical structures and is then suited to understand their amplification within the boundary layer. The numerical validation of the input/output method for the compressible case is given in appendix 1, where the same Reynolds number $Re = 232$ as the one studied by Ran *et al.*[26] is investigated for a low Mach number $M_\infty = 0.3$. The Reynolds number is now set to $Re = 180$ to always be below the critical Reynolds numbers for both the first and second modes for all cases, in agreement with equation (7).

The distribution of the receptivity coefficient for $M_\infty = 0.3$ is shown in figure 3(a). As depicted, the receptivity coefficient C_R shows two peaks, the first one associated with the emergence of streaks located at $\mathbf{k} = (0, 0.25)$ and the second one associated with the excitation of the TS waves located at $\mathbf{k} = (0.19, 0)$. These results are in good agreement with those provided by Ran[26] for the incompressible case. In particular, the contours of $\log_{10}(C_R)$ are well recovered using the low Mach number approximation (see also appendix 1).

Having approved the numerical approach chosen for a near incompressible Mach number, the receptivity coefficient C_R is re-computed for $M_\infty = 2$, 3 and 4.5 and depicted in figure 3(b)–(d). For

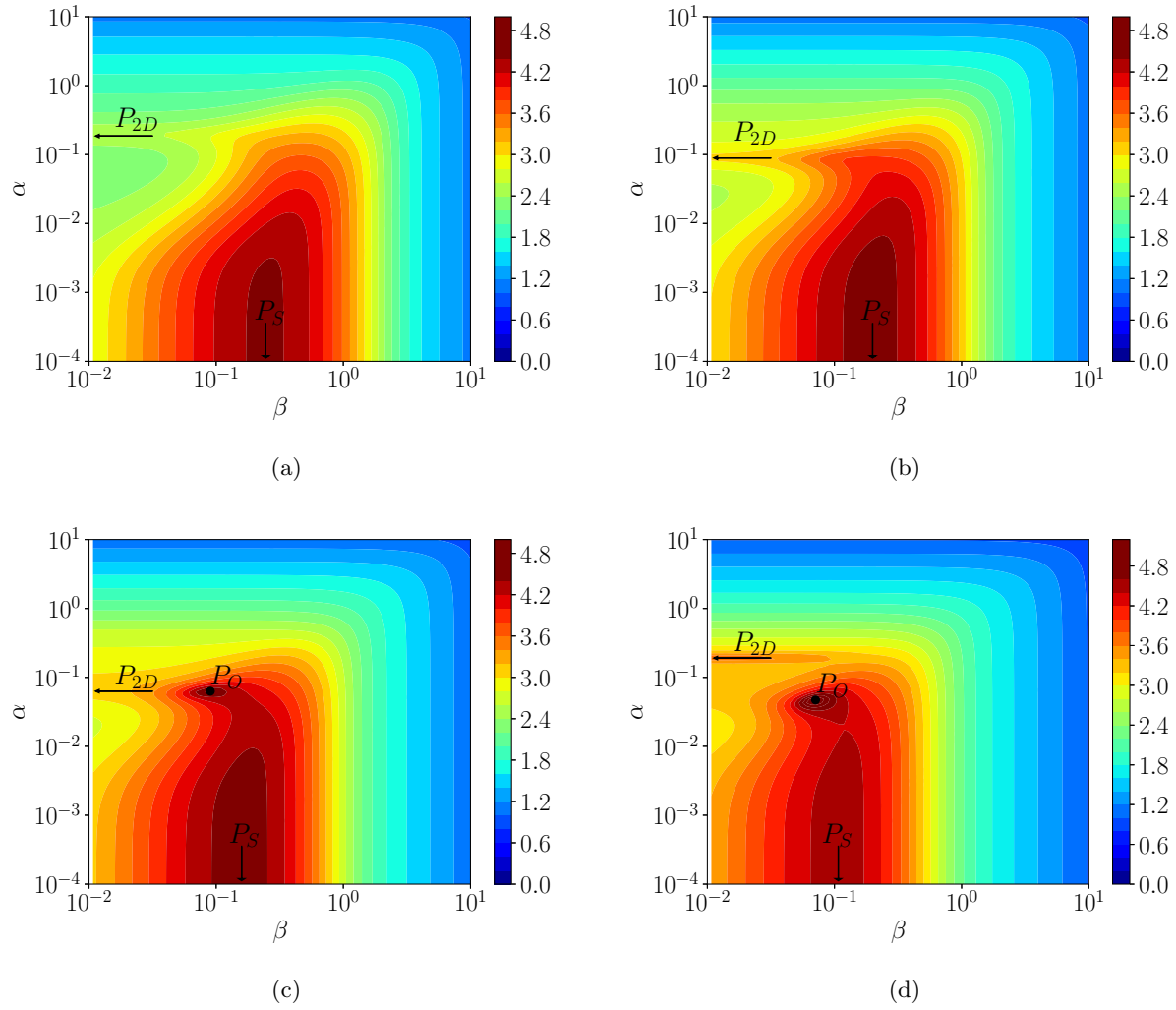

FIG. 3: Plots of $\log_{10}(C_R(\alpha,\beta))$ for (a) $M_\infty = 0.3$, (b) $M_\infty = 2$, (c) $M_\infty = 3$ and (d) $M_\infty = 4.5$. The Reynolds number is fixed to $Re = 180$. The peaks are indicated by arrows and a dot.

clear identification, the different peaks appearing in the receptivity plots are referred to as follows: P_{2D} is associated with the peak for β approaching zero (*i.e.* for $2D$ perturbation); P_O marks the wavenumber pair for the peak that corresponds to a purely oblique pattern ($\alpha \neq 0$ and $\beta \neq 0$); P_S is obtained at $\alpha \approx 0$ (*i.e.* the excitation of streaks). Note that this terminology is employed to avoid any confusion with a modal approach. Indeed, the nonmodal response corresponding to P_O, for instance, could be attributed to the contribution of several modes.

Depicted in figure 3(b), the $M_\infty = 2$ case exhibits a double peak structure similar to that observed for the nearly incompressible case at $M_\infty = 0.3$ in panel (a). However, the maximum of the receptivity coefficient is higher than its low-Mach number counterpart and is obtained for

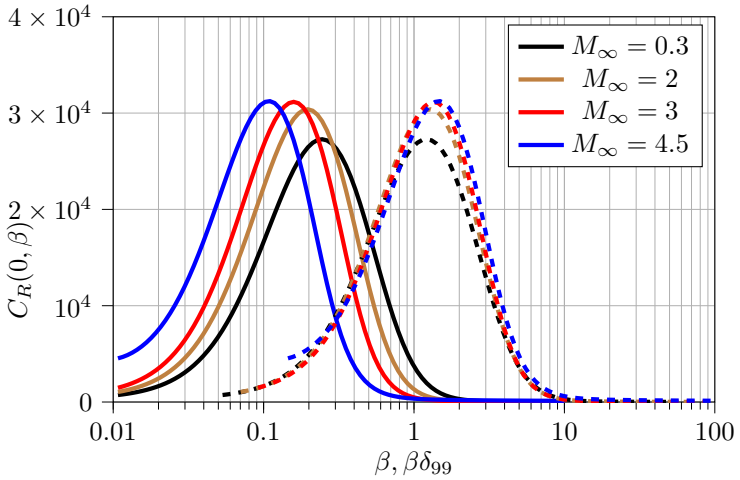

FIG. 4: Distribution of $C_R(0,\beta)$ for the different Mach numbers and $Re = 180$. Full line: the reference length $l = \sqrt{\mu_\infty x/(\rho_\infty U_\infty)}$ is used, in dashed lines data are rescaled with the δ_{99} boundary layer thickness.

wider spanwise scales. Especially, as the Mach number is increasing, the spanwise wavenumber corresponding to P_S is decreasing; the same observation was made by Hanifi *et al.*[10] for the optimal transient energy growth. In figure 4, we plot the distribution of the receptivity coefficient as a function of β for $\alpha = 0$ for the different Mach numbers. The peak corresponds to P_S. We also show $C_R(\alpha = 0, \beta\delta_{99})$. We may observe an almost universal scaling, independently of the Mach number, when data are rescaled with the δ_{99} boundary layer thickness. It seems quite intuitive that the size of streaks is correlated with the spatial extent of the boundary layer (and thus δ_{99}).

In comparison with the subsonic case, the P_{2D} peak for $M_\infty = 2$ is obtained at a smaller streamwise wave number (see figures 3(a,b)). Note that for $M_\infty = 2$ the maximum value obtained for C_R appears at $\alpha = 0$ (*i.e.* 2D wave) while the critical Reynolds number is found for an oblique wave, see figure 2. Besides, the receptivity coefficient P_{2D} reaches larger values than those reported for $M_\infty = 0.3$. A comparison of the nearly two-dimensional disturbances shows a similar distance between a real frequency forcing (*i.e.* axis $\omega_i = 0$) and the TS mode (or first mode for the supersonic flow) (not shown here). Hence, the increase of C_R in the neighborhood of the first mode can be attributed to non-normal effects where the forcing frequency is 'off-resonance', but the system can still exhibit a large response[24]. For the $M_\infty = 3.0$ and $M_\infty = 4.5$ cases in panels (c) and (d) of figure 3, respectively, the receptivity coefficient exhibits a third peak for oblique flow patterns (P_O). In particular, P_O is obtained for the couple $(\alpha, \beta) = (0.047, 0.071)$ for $M_\infty = 4.5$ corresponding to an angle of $\xi \approx 60^o$. This value is in fair agreement with the value reported

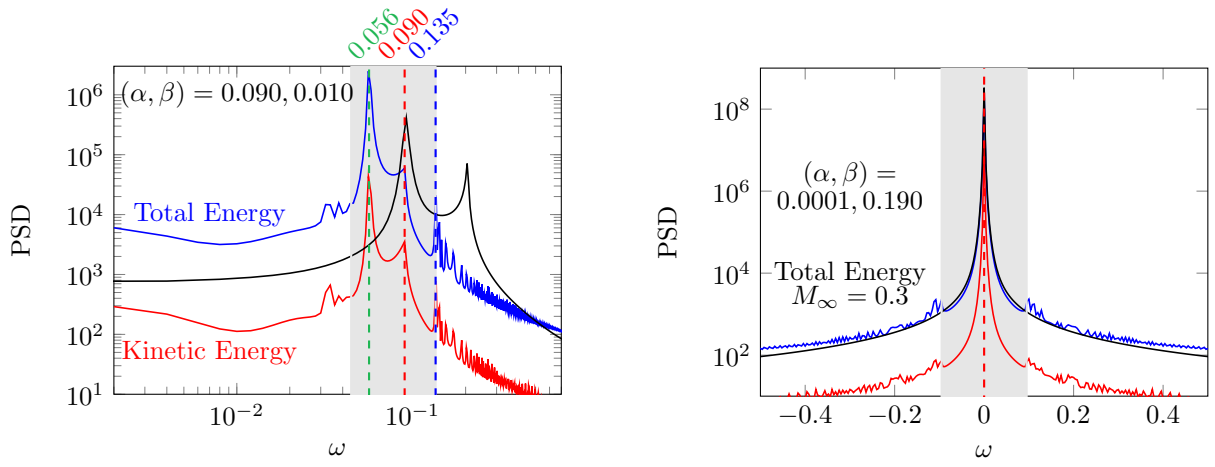

(a) (b)

FIG. 5: $M_\infty = 2$ and $Re = 180$. Power spectral density plots for (a) 'oblique pattern' $(\alpha, \beta) = (0.090, 0.010)$ and (b) 'streaks' $(\alpha, \beta) = (0.0001, 0.190)$. Frequencies of the first mode and second mode are depicted as green and blue vertical dashed lines, respectively. The frequency corresponding to the continuous branch is depicted as a red vertical dashed line. The total energy and kinetic energy contributions are shown in blue and red, respectively; the black colored $M_\infty = 0.3$ case is shown for comparison. The subsonic frequency range is shaded in grey.

in section 3.1 for the modal analysis. Interestingly, for $M_\infty = 3$, 2D perturbations (*i.e.* $\beta = 0$) exhibit larger values of C_R compared to the lower Mach number flow cases. Considering that the critical Reynolds number associated with the first mode for perturbations restricted to the (x, y) plane is increased from 300 to 570 when the Mach number varies from 2 to 4.5 (see figure 2), the increase in the receptivity coefficient can mainly be ascribed to non-normal effects (*i.e.* which are not proportional to the distance between the mode and real axis $\omega_i = 0$). Besides P_O, figure 3 shows the emergence of a distinct 2D peak for $M_\infty = 4.5$; the contribution of the second mode onto P_{2D} will be discussed below. Finally, the magnitude of C_R inside the region dominated by streaks contribution is almost independent of the Mach number.

3.2.2. Power spectral densities

In the above discussion, we consider the forcing (input) as a stochastic process. As a consequence, the response (output) is also driven through a stochastic organization. While this framework more clearly fits with the case of a boundary layer exposed to free-stream turbulence for instance – in comparison with previous studies limited to a single mode for the output or focusing

on response to harmonic forcing – it does not bring any information onto the spectral content of the response. In an effort to identify temporal frequencies which emerge from a broadband source of excitation, the power spectral densities (PSDs) for the different peaks observed in the receptivity coefficient maps are investigated in the following. To do so, we closely follow the theoretical framework described in section 2.3, in particular, we will consider two different operators $\mathbf{C}$. For the first choice, the output is based on velocities, temperature and pressure components, whereas the second choice includes only the velocity fields and the inner product is restricted to the kinetic energy. In this way, a clear characterization of the contributions of temperature and velocity fields to the response is enabled.

Depicted in figure 5, the PSDs are shown for $M_\infty = 2$ and (α, β) pairs corresponding to P_O and P_S, see figure 3(b). Frequencies which correspond to the first and second modes in the spectrum are depicted as green and blue dashed lines, respectively. The position of the continuous branch in the spectrum where $\omega/\alpha = 1$ is depicted as a red dashed line. The subsonic area extends from ω_- and ω_+ and is shaded grey. For comparison purposes, also the subsonic $M_\infty = 0.3$ case introduced above is added in figure 5 as a black line. As depicted in figure 5(a) for $M_\infty = 2$, the peak in the total energy is obtained at frequencies that match the first mode and the continuous branch, compare the green and red dashed vertical lines at $\omega = 0.056$ and 0.090. The peaks in the total energy and kinetic energy are located at almost identical ω, although the kinetic energy contribution is largely decreased for the increased Mach number. Besides these modes, the PSD associated with $M_\infty = 2$ exhibits secondary peaks near the supersonic region borders; one of those peaks correspond to the frequency of the second mode in the spectrum. At low frequencies, the PSD for $M_\infty = 2$ and P_{2D} exhibits a moderate contribution. For the subsonic $M_\infty = 0.3$ case, the two peaks associated with the first mode and the continuous branch are shifted to higher ω values. The contribution of the total energy at low frequencies is lower compared to the $M_\infty = 2$ case. Depicted in figure 5(b), the same study is repeated for the infinitely elongated structures in the streamwise direction. While the PSDs for both Mach numbers are almost superimposed when the output is based on the total energy of the fluctuations, a notable part of the total energy is transferred from the kinetic energy to the internal energy at $M_\infty = 2$, as also discussed for the streaks in[34]. In figures 5 and 6, one may observe that the PSDs exhibit several peaks in the supersonic range. This oscillatory part is associated with pseudo resonances of the acoustic modes in the spectrum. Similar behaviour is observed by Dawson & McKeon[32] for supersonic turbulent boundary layers.

Following the same notation as in figure 5, the PSDs for $M_\infty = 4.5$ are shown for $(\alpha, \beta) =$

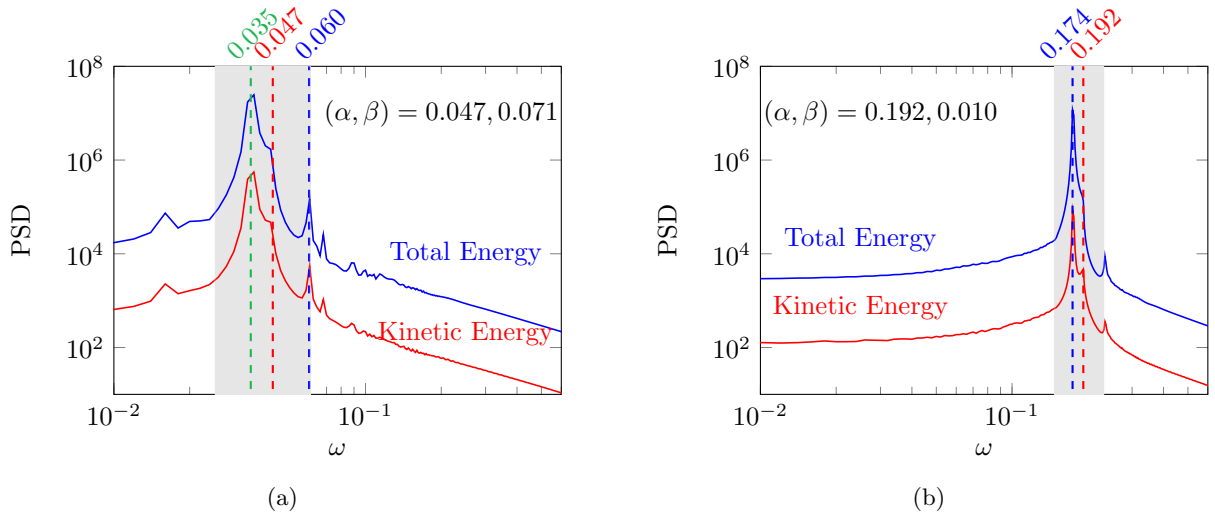

FIG. 6: $M_\infty = 4.5$ and $Re = 180$. Power spectral density plots for (a) $(\alpha, \beta) = (0.047, 0.071)$ and (b) $(\alpha, \beta) = (0.192, 0.010)$. The vertical lines correspond to $\omega = 0.047,\ 0.060$ and 0.035 in (a) and $\omega = 0.174,\ 0.192$ in (b). For color legends see figure 5.

$(0.047, 0.071)$ and $(\alpha, \beta) = (0.192, 0.010)$ in figure 6. The pairs of (α, β) are chosen to match the P_O and P_{2D} peaks in the receptivity coefficients, respectively, compare figure 3(d). The P_S peak associated with streaks will be discussed later on.

We first discuss the PSD associated with P_O; see also figure 1 for the corresponding spectrum. For this case, the least damped mode corresponds to the first mode and its PSD almost follows the same trend as the one observed for the 2D peak at $M_\infty = 2$. For both cases, the dominant peak in the power spectrum is associated with the first mode. However, for $M_\infty = 4.5$, the second mode is shifted towards the subsonic zone, see figure 1, which implies a near resonance in the PSD as shown in figure 6(a) where a distinct peak is observed near $\omega_r \approx 0.060$ (indicated in blue in the figure). Hence, it seems to play a role in the stochastic response for the oblique case.

The PSD for the almost two dimensional peak is depicted in figure 6(b). For this flow structure, the receptivity seems to be a consequence of a near resonance of the second mode with also a significant contribution of the continuous branch. Besides, the PSD exhibits an additional peak near the fast acoustic waves ($\omega_r \approx 0.235$). It should be indicated that additional stable Mack modes contribute into the stochastic response of P_{2D}, which all are inherently included in the present framework due to its stochastic approach. However, further analyses are needed to make a definite statement on their effective role. In consequence, this study shows the interest of combining both the stochastic framework and the resolvent analysis[29] to emphasize the most relevant spatial

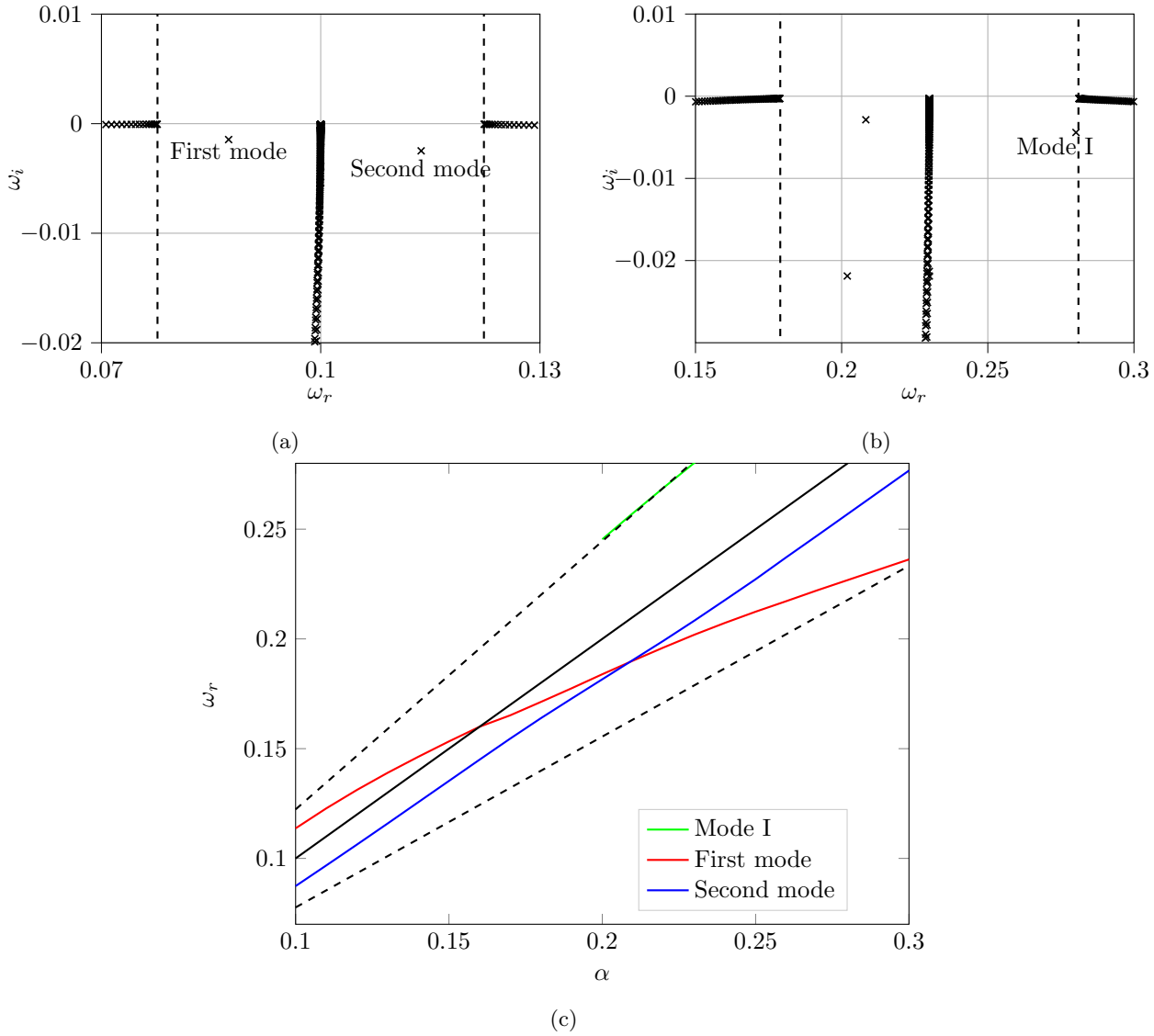

FIG. 7: $M_\infty = 4.5$ and $Re = 180$. (a) and (b) spectra for $\alpha = 0.10$ and $\alpha = 0.23$, respectively and $\beta = 0$. Panel (c) dispersion relations for the first and second modes. The discrete additional mode I (see panel (b)) is also shown. The slow and fast acoustic waves positions are represented by dashed lines. In (c), the position of the continuous branch is shown in black line.

scale due to white noise forcing and its associated spectral content which overcomes the limitations of previous theoretical receptivity studies (see Fedorov[21]) restricted to a single mode for the output.

To further identify the mechanism behind the observed amplification, the circular frequency ω_r as a function of the streamwise wave number α is depicted in figure 7(c) for the first and second modes; the spectra for $\alpha = 0.10$ and $\alpha = 0.23$ are given in panels (a,b). In accordance with figure 1, vertical dashed lines indicate the position of slow and fast acoustic waves for both spectra. As

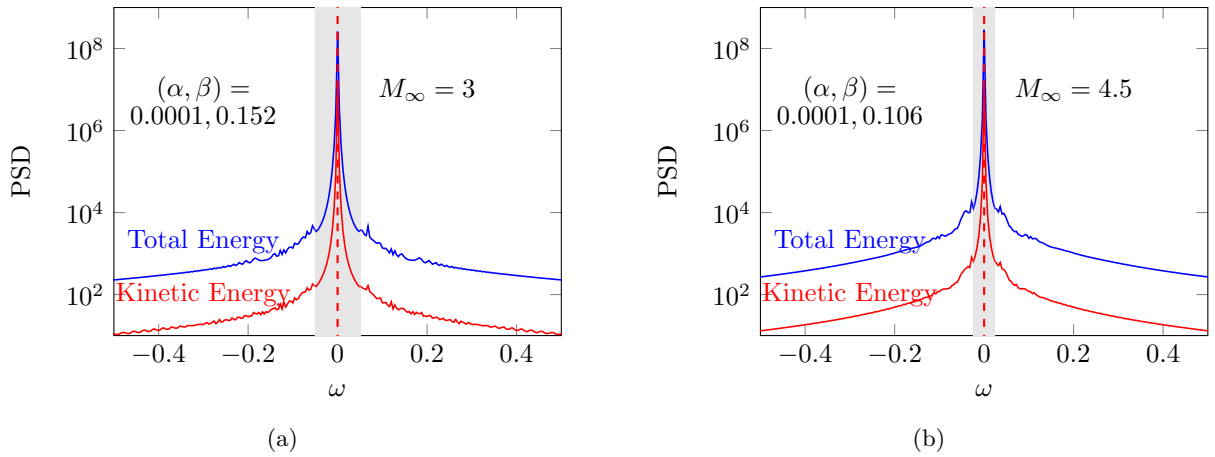

FIG. 8: $Re = 180$. Power spectral density plots for (a) $(\alpha, \beta) = (0.0001, 0.152)$, $M_\infty = 3$ and (b) $(\alpha, \beta) = (0.0001, 0.106)$, $M_\infty = 4.5$. For color legends see figure 5.

shown in figure 7(c), the frequencies and wave numbers of both the first and second mode coalesce for $\alpha \approx 0.2$, implying that modes are synchronized. The corresponding streamwise wavenumber appears close to the one associated with the peak P_{2D} ($\alpha \approx 0.19$). In the neighborhood of this region, the coupling leads to a strong amplification of the P_{2D} peak. It supports Fedorov's results[21] which established that the receptivity of the 2D mode is due to the synchronization of slow and fast modes (*i.e.* first and second modes). Furthermore, we also observe in spectrum 1(b) an additional mode emerging from the fast acoustic branch of modes. Ma & Zhong[16] have referenced this additional mode as mode I. For the latter, the variation of ω_r with α is shown in figure 7(c). For $\alpha \approx 0.2$, mode I becomes synchronized with the fast acoustic wave. It may support the role played by the additional stable mode I in the amplification of the receptivity coefficient as underlined by Ma & Zhong[16].

Finally, for the sake of completeness, figures 5(b) and 8 show the influence of Mach number on the receptivity of the streaks. The figures show a nearly equal energy distribution in the frequency domain for all considered Mach numbers implying that the general behavior of the streaks is essentially Mach number invariant.

3.2.3. Input/output components of the receptivity for $M_\infty = 4.5$

In the previous section, the disturbances introduced into the boundary layer were restricted to the velocity field, assuming that all velocity components penetrate the boundary layer simultaneously with the same magnitude. In reality, however, perturbations typically exhibit a preferential

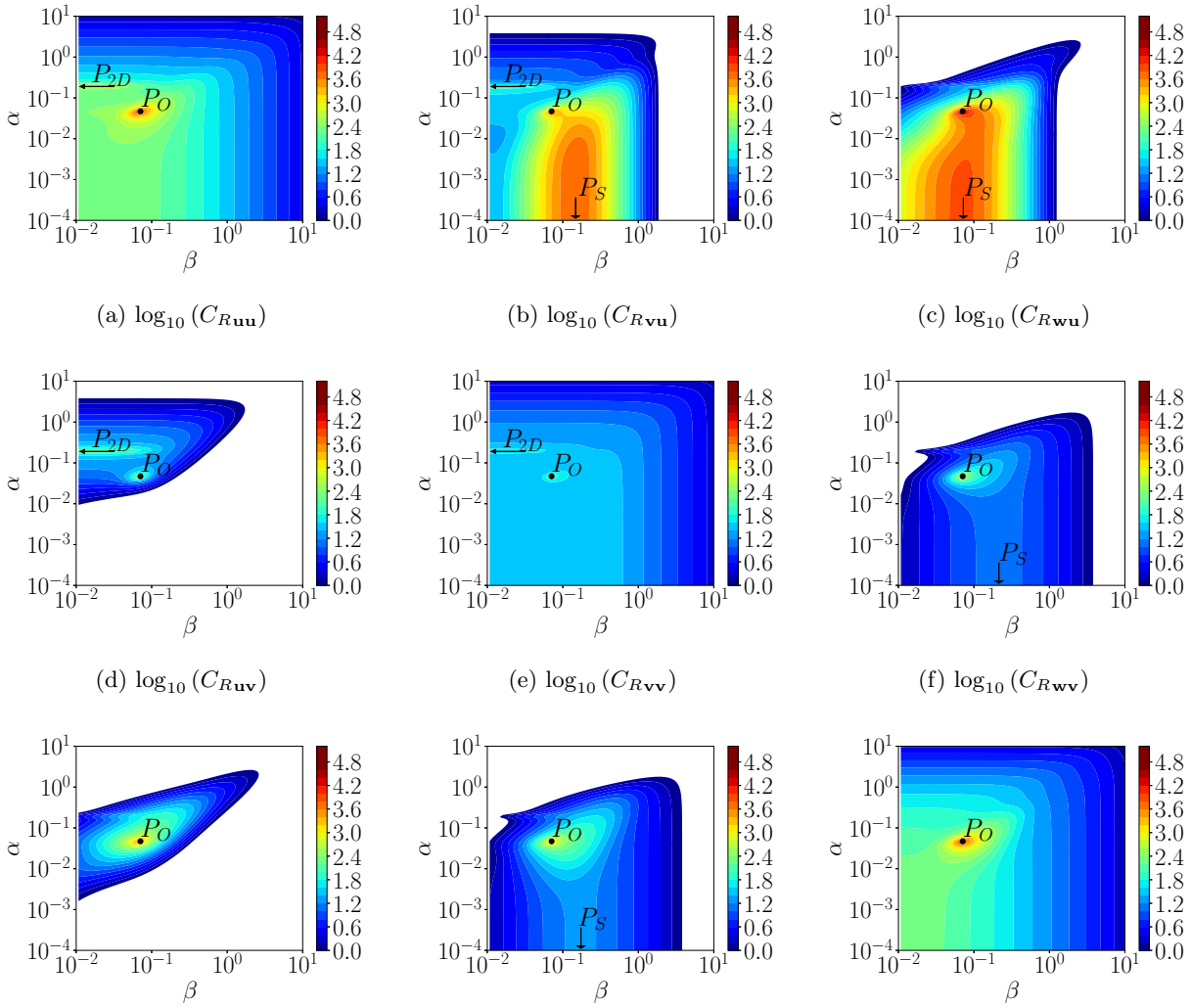

(a) $\log_{10}(C_{R\mathbf{uu}})$ (b) $\log_{10}(C_{R\mathbf{vu}})$ (c) $\log_{10}(C_{R\mathbf{wu}})$

(d) $\log_{10}(C_{R\mathbf{uv}})$ (e) $\log_{10}(C_{R\mathbf{vv}})$ (f) $\log_{10}(C_{R\mathbf{wv}})$

(g) $\log_{10}(C_{R\mathbf{uw}})$ (h) $\log_{10}(C_{R\mathbf{vw}})$ (i) $\log_{10}(C_{R\mathbf{ww}})$

FIG. 9: Plots of the receptivity coefficients for the velocity components and $M_\infty = 4.5$. The subscripts indicate the input/output couple that is selected. For instance, the subscript **wu** indicates that **w** is the input and **u** is the output. White regions are associated with levels below 0.

direction, e.g., wall-normal blowing/suction mainly affects the wall-normal velocity component, and in the compressible regime, also the temperature field serves as a potential input. In this section, the dependence of the receptivity coefficient C_R on the different input/output field components, also including temperature perturbations, is investigated for the same range of spatial wavenumbers for a supersonic Mach number of $M_\infty = 4.5$, where compressibility effects are substantial. To this end, we will adopt/extend the input-output technique described in Jovanović & Bamieh[27] for

incompressible channel flows to the compressible boundary layer case, which is the first time to the best of the author's knowledge. This way, components with the most significant influence on the selected streamwise and spanwise scales can be easily identified. Hereafter, C_{Rij} denotes the receptivity coefficient associated with the input $\mathbf{d}_i$ and output $\mathbf{q}_j$ where $ij \in (\mathbf{u}, \mathbf{v}, \mathbf{w}, \boldsymbol{\theta})^2$. As in the previous section, perturbations are introduced through the whole height of the boundary layer, see section 3.2.1.

Plotted in the same representation as in figure 3, the dependence of the receptivity coefficient $C_{Ri\mathbf{u}}$ on the forcing component $\mathbf{d}_i$ is depicted in figure 9(a)–(c). At first the receptivity of the streaky motion P_S with $\alpha \approx 0$ (*i.e.* mainly governs by $\mathbf{q_u}$) is discussed. In accordance with the findings pointed out by Jovanović & Bamieh[27] for the incompressible channel flow case, the wall-normal and spanwise forcing in panels (b) and (c) show a much stronger influence than the streamwise velocity forcing in panel (a). Additionally, when the input is restricted to $\mathbf{d_w}$ (panel (c)) the excitation of streaks is optimal for a spanwise length which is twice as wide as the one obtained by forcing the wall-normal velocity (panel (b)). Streaks footprint can also be observed to a lesser extent for the outputs $\mathbf{q_v}$ and $\mathbf{q_w}$ for inputs $\mathbf{d_w}$ and $\mathbf{d_v}$, respectively (see panels (f) and (h)).

For P_O, the measurements which reach the strongest amplitude are mainly associated with inputs restricted to either the streamwise or spanwise velocity component. Especially, the stochastic response for P_O peaks with values that are at least of the same order of magnitude than for the streaks, (see panel (c) for instance). This implies that the oblique wave transition scenario may come to dominate over the one involving rolls and streaks. For the excitation of the 2D flow structure, the streamwise velocity forcing has the most impact onto the variance associated with P_{2D}. However, its amplification is significantly weaker than that achieved by either the oblique pattern or streamwise infinitely elongated streaks. Finally, characteristic length scales for both P_O and P_{2D} are seen to be only marginally dependent of the choice for the input and output velocity component.

In figure 10, the effect of the temperature field onto C_R is illustrated; i.e., panels (a)–(c) give the influence of the various components of the velocity perturbations on the temperature output, panels (d)–(f) the influence of the temperature perturbations on the various velocity components for output. Comparing panel (b)–(c) with (d), it is apparent that the variance of temperature perturbation plays mainly a passive role for the streaks (*i.e.* the temperature disturbance acts as a passive scalar). Indeed, forcing θ has no effect on the streamwise velocity in the range of spanwise and streamwise wavenumbers corresponding to the amplification of the streaks. This

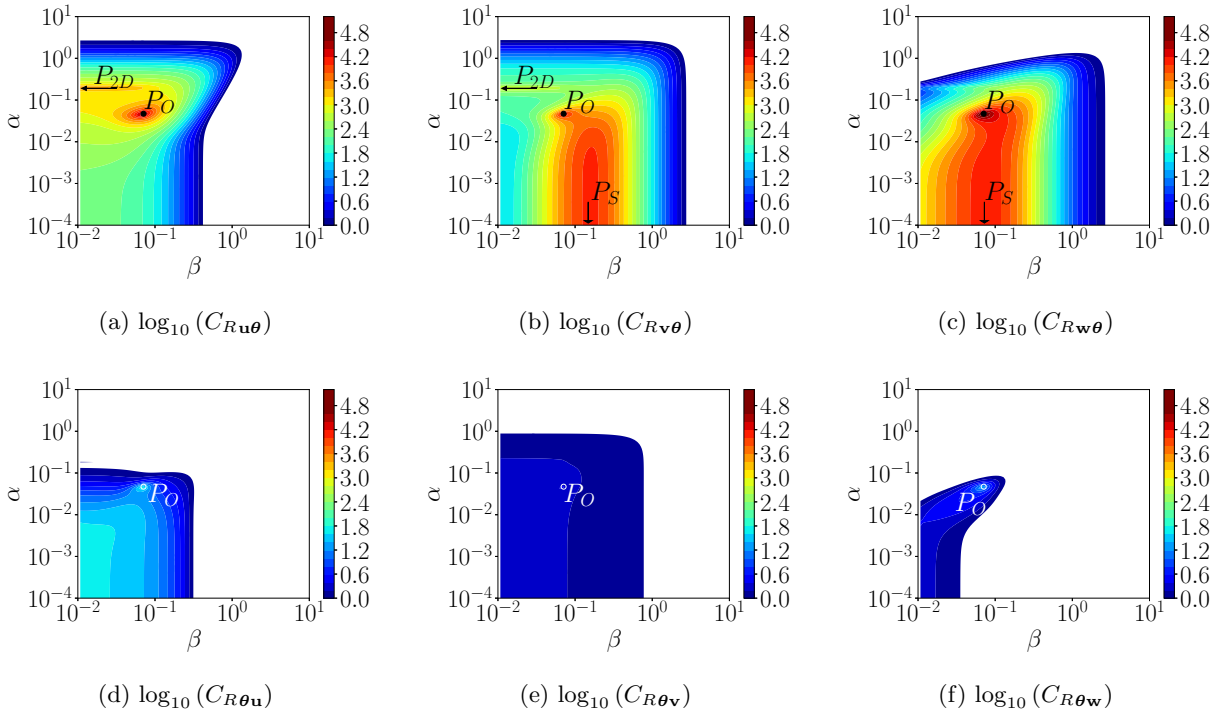

(a) $\log_{10}(C_{R\mathbf{u}\boldsymbol{\theta}})$ (b) $\log_{10}(C_{R\mathbf{v}\boldsymbol{\theta}})$ (c) $\log_{10}(C_{R\mathbf{w}\boldsymbol{\theta}})$

(d) $\log_{10}(C_{R\boldsymbol{\theta}\mathbf{u}})$ (e) $\log_{10}(C_{R\boldsymbol{\theta}\mathbf{v}})$ (f) $\log_{10}(C_{R\boldsymbol{\theta}\mathbf{w}})$

FIG. 10: Plots of the receptivity coefficients for the velocity and temperature components and $M_\infty = 4.5$. For details, see caption in figure 9.

remark is consistent with recent results provided by Madhusudanan & McKeon[34]. On the other hand, forcing streamwise vortices (including both spanwise and wall-normal velocity components) leads to amplify streaks of temperature, see panel (b) and (c). In particular, the range of α and β where the temperature component achieves its maximum is similar to those obtained for the streamwise velocity output as shown in figures 9 (b,c). Similar conclusions can be drawn for the role of the temperature onto the excitation of the 2D peak (P_{2D}). For the latter, figures 10(a,b) show that the streamwise velocity forcing in panel (a) is the most efficient input to amplify its temperature component. At the opposite, an active role of the temperature fluctuation is found for the excitation of the oblique structure, as the peaks in intensity observed in panels (d) and (f) for P_O indicate. It suggests the effectiveness of a laser perturber used experimentally for generating a temperature spot with the objective to amplify instability waves[35].

3.2.4. Influence of input wall-normal positions onto receptivity coefficients

In the previous sections, the random number-based input was introduced over the entire height of the boundary layer, which thus gives a very complete impression of the boundary layer response

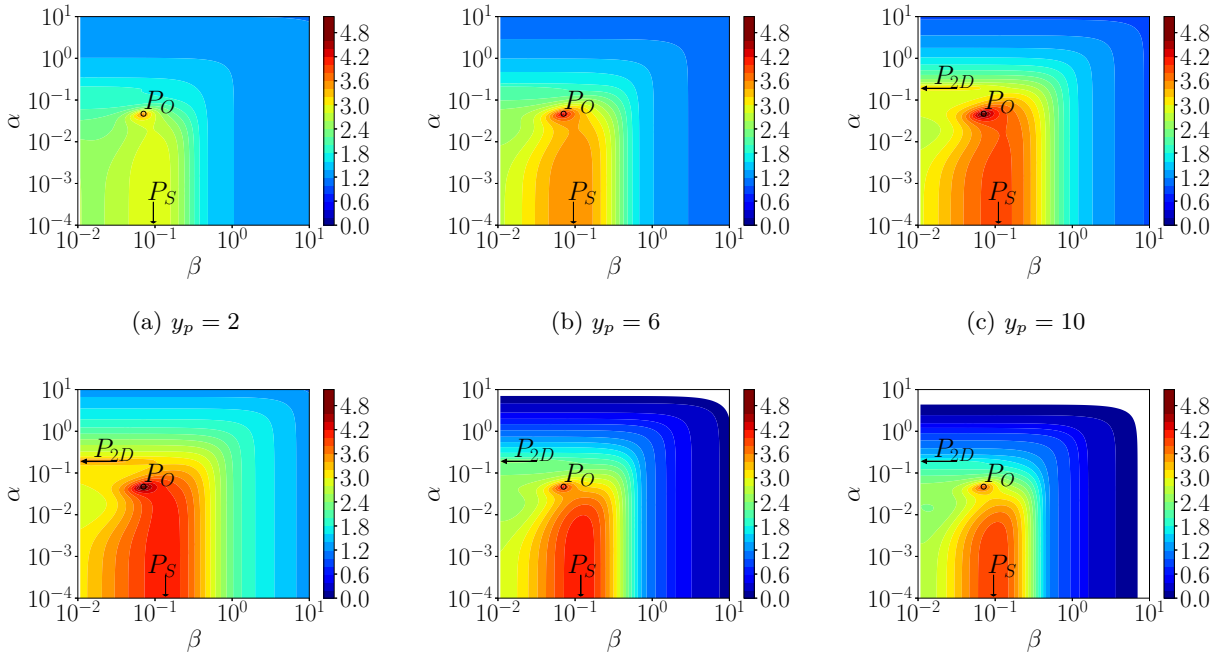

(a) $y_p = 2$ (b) $y_p = 6$ (c) $y_p = 10$

(d) $y_p = 14$ (e) $y_p = 18$ (f) $y_p = 22$

FIG. 11: Plot of the receptivity coefficients in a logarithmic scale as a function of the wall-normal position associated with the forcing for $M_\infty = 4.5$. The δ_{99} boundary layer thickness is located at $y = 13.6$.

associated with a given input. In reality, however, external perturbations, such as wall blowing and suction, free-stream turbulence, roughness elements often penetrate the boundary layer only in either the near-wall region or the outer region, which is known to cause a significantly different response of the boundary layer. Allowed by the great flexibility of the framework formulation chosen, see Ran *et al.*[26] for an incompressible point of view, we will investigate how the forcing position along the wall-normal direction influences the receptivity mechanisms in the compressible regime for the first time to the author's best knowledge.

For that purpose, a series of computations with a localized forcing $\mathbf{f}$ (11) is conducted at $M_\infty = 4.5$, for which the maximum value along y is progressively increased. Hereafter, $y_2 - y_1 = 2$, $a = 10$ and we note $y_p = (y_2 + y_1)/2$. The input and output include velocities, pressure and temperature components. The measurement is restricted within the boundary layer δ_{99} thickness, for this case, the wall-normal position where $\delta_{99} = 1$ is located at $y = 13.6$. The receptivity coefficient as a function of y_p is plotted in figure 11. It is observed that near wall forcing generates mainly oblique flow structures, compare panels (a) and (b). When the input is shifted upwards, the boundary

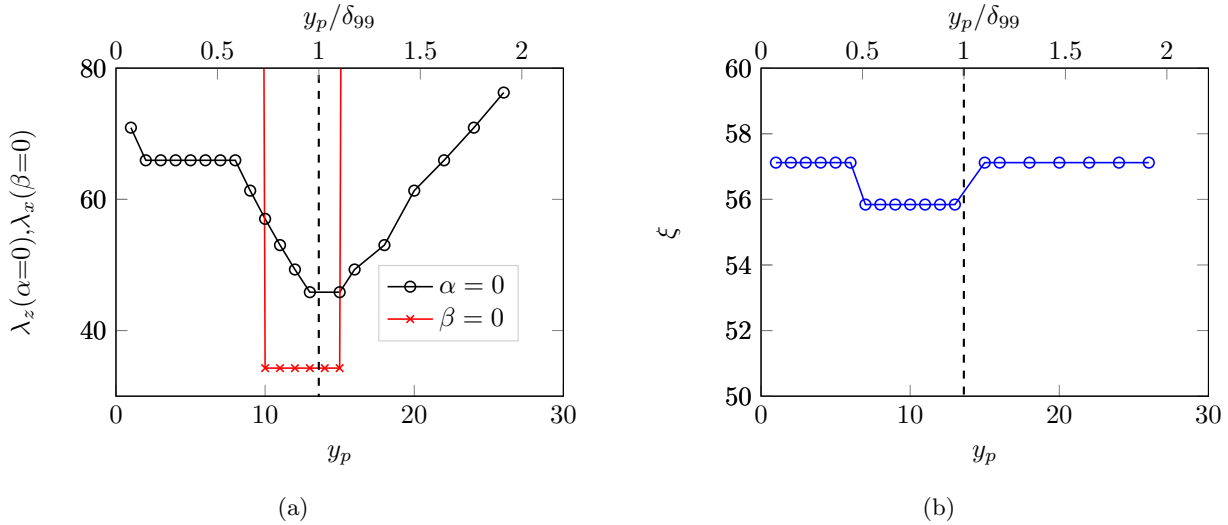

FIG. 12: Flow structure characteristics as a function of the wall-normal position of the forcing y_p for $M_\infty = 4.5$. (a) Characteristic wavelengths $\lambda_z = 2\pi/\beta$, $\lambda_x = 2\pi/\alpha$ for streaks and 2D flow structures ($\alpha = 0$ and $\beta = 0$, respectively). The position of the δ_{99} boundary layer thickness is shown in vertical dashed lines. (b) angle $\xi = \arctan \beta/\alpha$ for the oblique pattern.

layer streaks get strongly amplified. As the forcing region comes closer to the boundary layer edge, compare panels (c) and (d), also the excitation of 2D patterns is noted. The location at which the energy peaks is found close to the boundary layer edge for either 2D and oblique flow structures or streaks. On the other hand, when the forcing shifts in the freestream, the energy amplification decreases for all flow structures even if its noticeably less pronounced for streaks and oblique patterns. Note that the characteristic spanwise length associated with streaks changes with y_p.

The behaviours observed in figure 11 are summarized in figures 12 and 13 in an effort to synthetize the main conclusions. For that, we consider only streamwise and spanwise wavenumbers associated with peaks in total energy (*i.e.* P_O, P_{2D} and P_S). In figure 12(a), we show that the spanwise scale λ_z associated with streaks exhibits two distinct behaviours. For forcing regions inside the δ_{99} boundary layer thickness, we observe that streaks become shorter as y_p is increasing. For freestream excitation, the opposite behaviour is found. The upward shift in y_p gives rise to amplify wider streaky patterns with an almost linear dependency between λ_z and y_p. For the freestream forcing, a similar trend is reported by Ran *et al.*[26] for the incompressible flow case. For the 2D flow structure (*i.e.* $\beta = 0$), the maximum variance is concentrated in a narrow region along the wall-normal direction ($10 \leq y_p \leq 15$). Outside this area, peaks in total energy are obtained at

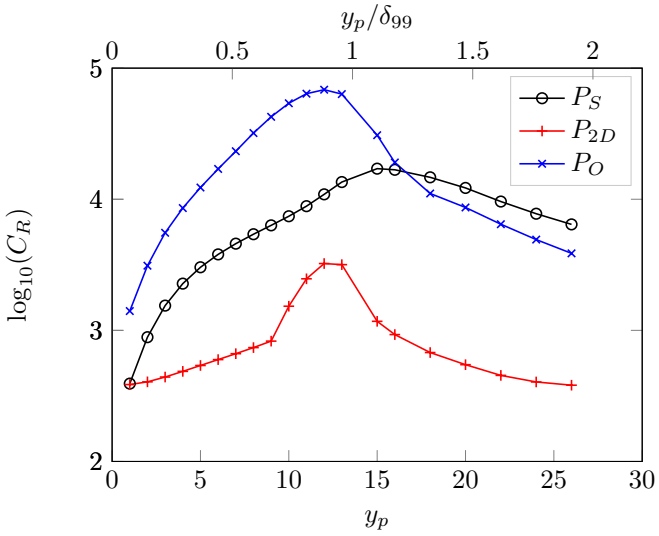

FIG. 13: Distribution of the receptivity coefficient in a logarithmic scale for P_{2D} (red), P_O (blue) and P_S (black) as a function of the wall-normal position of the input.

small values of α. It indicates that the 2D flow structure is optimally excited in this flow region. For the oblique pattern, we show that the orientation angle in the (x, z) is almost independent of y_p, see figure 12(b).

In figure 13, the distributions of the receptivity coefficient maxima along with y_p are depicted for the same flow structures. The figure shows that the range of wall-normal positions that produces the largest variance is $10 \leq y_p \leq 15$ for both oblique and 2D patterns. Especially, the peaks in the receptivity coefficient for both cases are located close to $y_p = 12$ near the edge of the boundary layer ($y_p \approx 13.6$). On the other hand, the maximum variance associated with streaks occurs for $y_p = 15$, above the boundary layer edge. Especially, for y_p larger than 16, the optimally stochastically excited flow structure is mainly driven by the streaks. For $y_p > 16$, the level of variance for both streaky and oblique flow structures decreases almost linearly with y_p. It further indicates a strong competition between the amplification of streaks and oblique flow structures when varying y_p which has not been pronounced in previous receptivity analysis regarding supersonic boundary layers that clearly[1].

Finally, the receptivity of the supersonic boundary layer to stochastic near-wall perturbations is studied for inputs restricted to either a velocity component or the temperature disturbance. For that, y_1 and y_2 are fixed to 0 and 2 in (11) and a is set to 10. In figure 14, the correlation maps indicate that both $\mathbf{d_v}$ and $\mathbf{d_u}$ can amplify the P_{2D} peak which is not in complete agreement with DNS results provided by Wang & Zhong[17]. Nevertheless, the freestream Mach number investigated

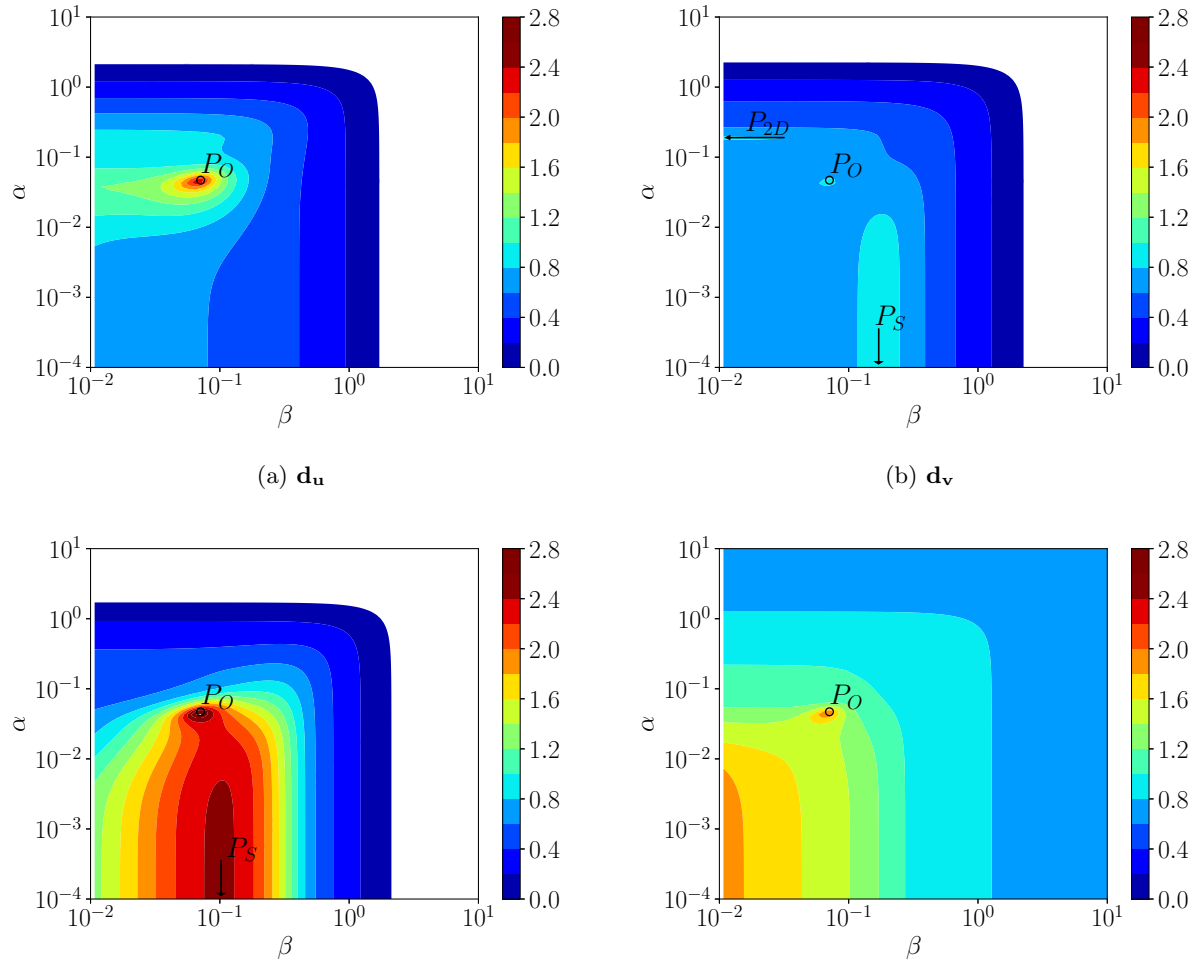

(a) $\mathbf{d_u}$ (b) $\mathbf{d_v}$

(c) $\mathbf{d_w}$ (d) $\mathbf{d_\theta}$

FIG. 14: Distribution of the receptivity coefficients in a logarithmic scale for various forcing components at $y_p = 1$ and $M_\infty = 4.5$.

by Wang & Zhong is fixed to $M_\infty = 5.92$ and we can not make definite statements regarding the Mach number effect. It is interesting to observe that spanwise near wall fluctuations have a prominent effect on the amplification of streaks and oblique patterns. In addition, temperature perturbation near the wall also leads to amplify the P_O peak.

3.2.5. POD response and forcing modes

While the previous sections provide insight into the streamwise and spanwise scales that emerge under a continuous stochastic excitation, it brings no information about the wall-normal distribution of the forced flow structures. This section is devoted to connect the different peaks found in

the receptivity coefficient maps to characeristic eddies and their wall-normal structures. For that, we investigate modes associated with a proper orthogonal decomposition (POD) of the correlation matrix hereafter.

For a clear understanding, we recall that the correlation matrix $\mathbf{X}_\infty$ has a positive definite Hermitian form with positive real eigenvalues. In particular, eigenvalues are associated with mutually orthogonal eigenvectors. Each eigenvector corresponds to a response flow pattern for which its contribution to the total variance is given by its corresponding eigenvalue. This decomposition is classically referred to as response (or direct) KL (Karhunen-Loéve) or POD (proper orthogonal decomposition) modes; hereafter, eigenvalues of $\mathbf{X}_\infty$ are noted σ_j. As a consequence, the variance of $\mathbf{X}_\infty$ is given by $\sum_j \sigma_j$. Then, the ratio $r_i = \sigma_i / \sum_j \sigma_j$ represents the contribution of the i_{th} POD mode to the total variance. In the same vein, we consider optimal forcing functions which are excited with equal probability and independently by a stochastic input. As for the response modes, the forcing flow structures can be ordered according to their relative contribution to the maintained total variance by stochastic excitation. These forcing modes constitute also a complete set of orthogonal functions that can be computed by solving the dual Lyapunov system of (3). They are referenced as back KL (POD) modes or forcing KL (POD) modes[22,25]. In figure 15(a), the distribution of r_1 in the (α, β) plane is displayed in which the response POD mode 1 is associated with the largest eigenvalue. The figure shows that flow structures associated with streaks, oblique pattern and the 2D flow structure are mainly driven by the first response POD mode that contributes to almost 90% of the total variance. A similar observation still holds for the forcing POD modes, see figure 15(b). One may recall that the total variance obtained by considering either the correlation matrix $\mathbf{X}_\infty$ or its dual is identical.

To give insight into the velocity/temperature coupling for the different receptivity coefficient maxima, we further investigate the dependency of the dominant forcing POD mode onto the measurement of the output variance. At first we want to investigate the excitation of streaks. As concluded from figure 9, streaky motions are mainly driven by a forcing restricted to either $\mathbf{v}$ or $\mathbf{w}$. For the sake of brevity, we only consider the wall-normal velocity component as an input in the following, however, similar conclusions can be drawn for the next discussion when considering the spanwise velocity component. Based on previous analyses and assuming an input limited to $\mathbf{v}$, the streaks are mostly amplified for $\beta \approx 0.15$ and $\alpha = 0$ for a forcing spatially extended within the δ_{99} boundary layer thickness, compare figure 9(b). To identify the role of the temperature, the output is either associated with the temperature field or the streamwise velocity components. The dominant response POD mode is now computed using the operator $\overline{\mathbf{C}}\mathbf{X}_\infty\overline{\mathbf{C}}^H$ and the dominant

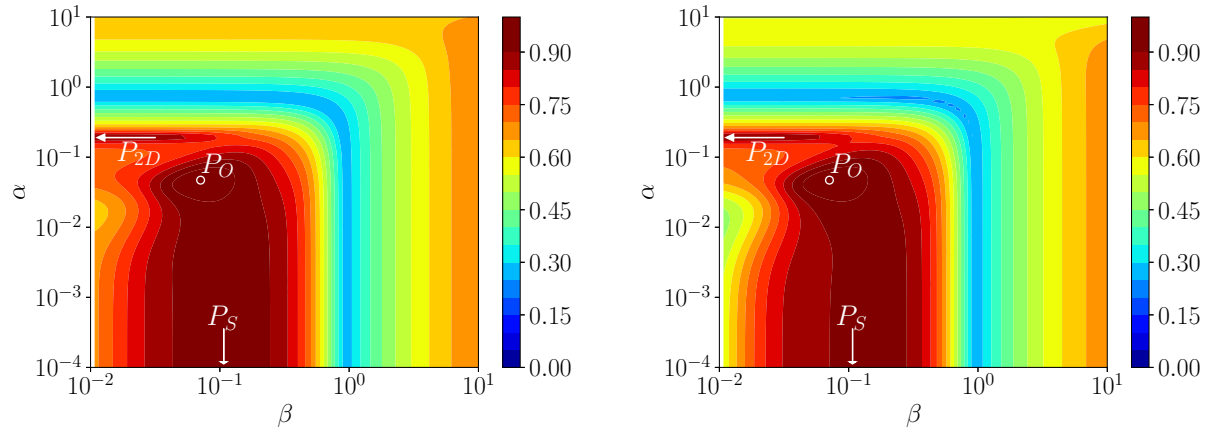

(a) (b)

FIG. 15: The distribution of $r_1 = \sigma_1 / \sum_j \sigma_j$ for response POD (a) and forcing POD (b) modes and $M_\infty = 4.5$. The subscript 1 refers to the largest eigenvalue of the correlation matrix (a) or its dual (b).

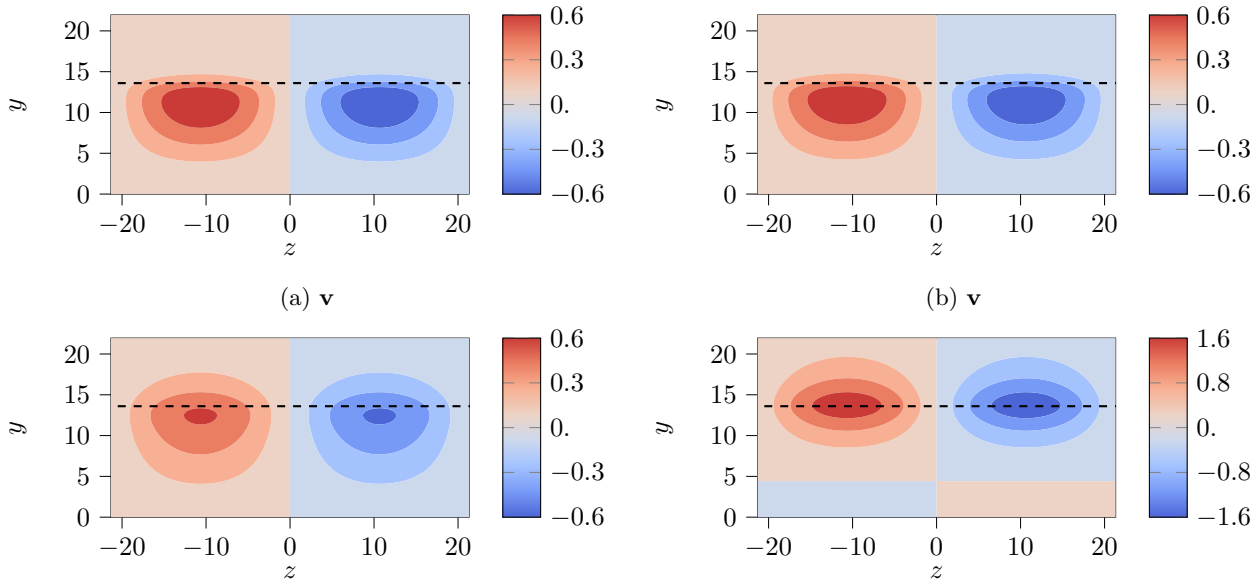

(a) **v** (b) **v**

(c) **u** (d) $\boldsymbol{\theta}$

FIG. 16: Dominant forcing (a,b) and response (c,d) POD modes for $(\alpha, \beta) = (0, 0.15)$, $M_\infty = 4.5$ and the input limited to **v**. The wall-normal velocity component is shown in (a,b). The streamwise velocity and temperature components are shown in (c,d), respectively. Panels (a,c) correspond to the output measurement restricted to **u**. Panels (b,d) correspond to the output measurement restricted to $\boldsymbol{\theta}$. The position of the boundary layer edge is shown in dashed lines ($y \approx 13.6$).

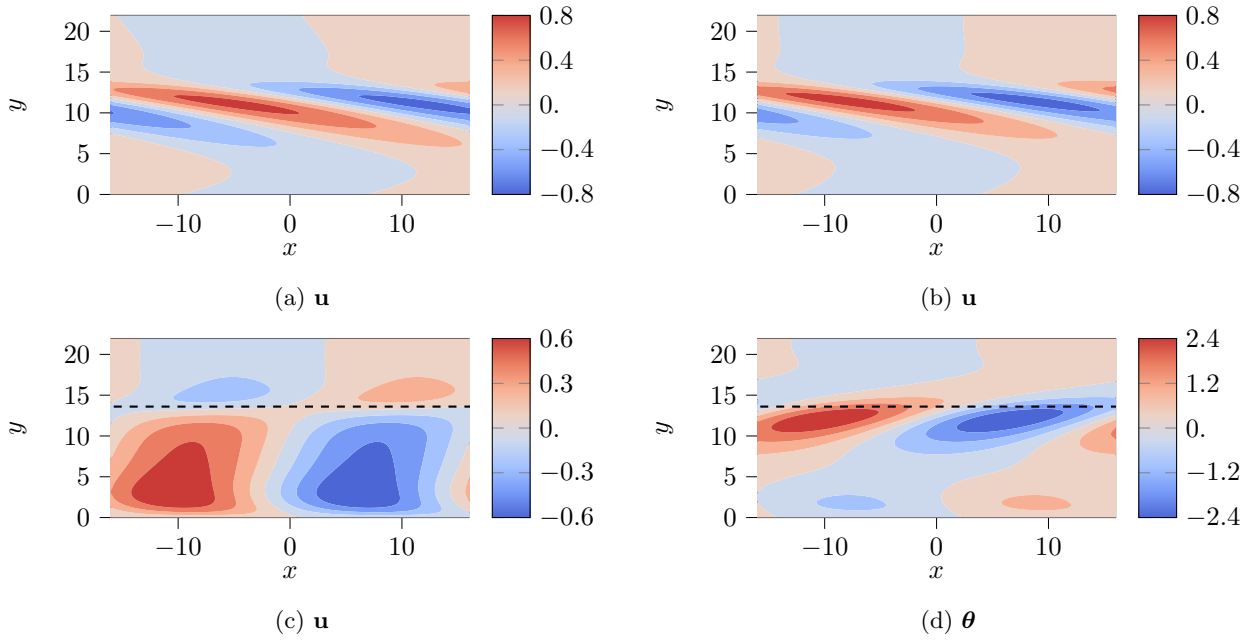

(a) **u** (b) **u**

(c) **u** (d) $\boldsymbol{\theta}$

FIG. 17: Dominant forcing (a,b) and response (c,d) POD modes for $(\alpha, \beta) = (0.19, 0)$, $M_\infty = 4.5$ and the input limited to **u**. The streamwise velocity component is shown in (a,b). The streamwise velocity and temperature components are shown in (c,d), respectively. Panels (a,c) correspond to the output measurement restricted to **u**. Panels (b,d) correspond to the output measurement restricted to $\boldsymbol{\theta}$.

forcing POD mode obtained by solving the dual system of (3).

In figure 16, the eigenfunctions associated with the dominant forcing/response POD mode for $\alpha = 0$ and $\beta \approx 0.15$ are shown. The figure shows that the forcing POD modes maximizing the output variance which is measured either on θ or u are quite the same. It illustrates the strong correlation between the temperature and velocity components for the streaks.

In figure 17, we show the dominant forcing and response modes for the 2D peak (*i.e.* P_{2D}) at $(\alpha, \beta) = (0.19, 0)$, compare figure 9(b). Two measurements are considered. The first choice is based on the streamwise velocity component, the second choice includes only the temperature θ. For both cases, only the streamwise velocity u is forced. The latter component will give rise to the optimal flow response for P_{2D}, see figures 9 and 10. The figure shows that the forcing distribution that produces the most variance exhibits a pattern inclined against the shear whatever the measurement considered. It indicates that amplification of P_{2D} which occurs at the synchronization of the first and second mode is enhanced by the Orr mechanism since we observe the flipping of the structure along the basic shear for the response mode.

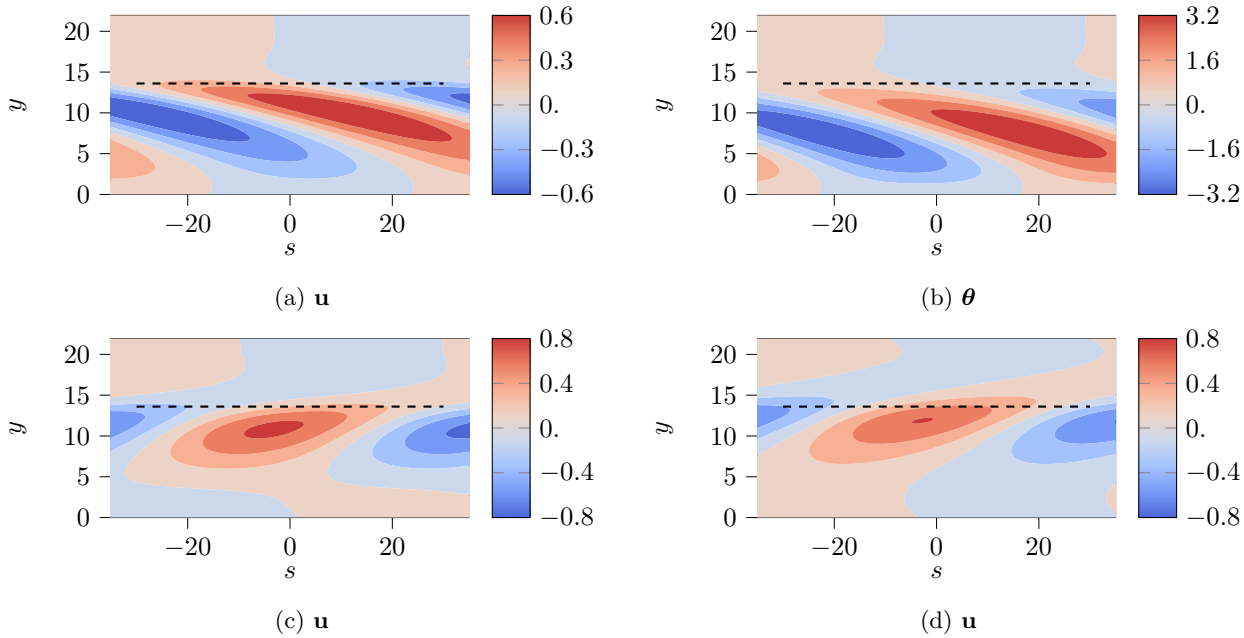

(a) **u** (b) $\boldsymbol{\theta}$

(c) **u** (d) **u**

FIG. 18: Dominant forcing (a,b) and response (c,d) POD modes for $(\alpha, \beta) = (0.04, 0.07)$, $M_\infty = 4.5$ and the measurement based on **u**. The streamwise velocity component is shown in (a,c,d). The temperature component is shown in (b). Panels (a,c) correspond to the input restricted to **u**. Panels (b,d) correspond to the input restricted to $\boldsymbol{\theta}$. The position in the wavevector direction is denoted by s.

In addition, the forcing appears to be almost independent of the output (either u or θ), indicating that the temperature fluctuation seems to play only a passive role for the P_{2D} peak. Finally, while the direct POD mode for the streamwise velocity component is localized within the δ_{99} boundary layer thickness, the direct POD mode associated with the temperature peaks near the edge of the boundary layer.

The same approach is conducted for the oblique pattern that corresponds to P_O; results are reported in figure 18. For this case, two inputs are investigated. The first one only includes the streamwise velocity contribution, the second input is based on the temperature disturbance. The measurement is restricted to the streamwise velocity component. We plot in figure 18 the forcing and response modes for σ_1 in a plane that includes the wavevector. The corresponding coordinates is noted s in the figure. The figure shows that the temperature can play an active role in triggering the oblique pattern. Especially, the distribution of the response POD mode appears to be independent of the input choice. In other words, the forcing restricted to θ leads to the same streamwise velocity measurement than the input associated with u only. Finally, the

dominant forcing POD mode is also dominated by tilting in the shear direction according to the Orr mechanism. On one hand, the forcing for both θ and u are mainly localized within the δ_{99} boundary layer thickness. On the other hand, the response POD mode is shifted away from the wall and peaks near the edge of the boundary layer.

4. SUMMARY AND CONCLUSIONS

This paper revisits the linear receptivity of the supersonic adiabatic laminar boundary layer by using an input/output framework based on the stochastically forced linearized compressible Navier-Stokes equations. The method thus extends the conceptually equivalent incompressible analysis of Ran *et al.*[26] to the compressible regime. To provide additional insights to results provided within a modal framework, a white-in-time stochastic forcing with an identity spatial covariance operator is considered as an input, which prevents a specific mode to be promoted for the output. Furthermore, the stochastic input can be selectively attributed to only one or various combinations of the flow field variables with a user-defined wall-normal distribution. Hence, the framework allows for a detailed investigation of the amplification of various flow patterns (either oblique or two-dimensional and streaks) which enables an understanding of the correlation between forcing and response flow structures.

Following the same approach as in the incompressible analysis, the receptivity coefficients computed from the input/output framework are analyzed for different Mach numbers (0.3 – 4.5) and different perturbation types. When decomposed into streamwise and spanwise wavenumbers α and β, respectively, three Mach-number dependent types of distinct peaks are illustrated corresponding to the enhancement of streaks (P_S), oblique flow structures (P_O), and 2D patterns (P_{2D}), which is in agreement with previous findings for the compressible regime.

As observed in the incompressible limit[27] and recently for compressible flow[34], the amplification of streaks is only driven by a forcing limited to the wall-normal and spanwise velocity components. For the amplification of the two-dimensional flow structure ($i.e\ \beta = 0$), the prominent role of forcing the streamwise velocity component is illustrated. While the role of the temperature fluctuation can be seen to be rather passive for both the streaks and 2D patterns for the Mach number cases considered, the excitation of oblique flow structure is significantly influenced by the temperature disturbances. This behaviour is consistent with the linear receptivity model derived by Fedorov & Tumin[35], even if the latter is restricted to the excitation of only the first mode. This deserves particular emphasis inasmuch as the power spectral densities show that the amplification for all

peaks appears to be the result of several frequencies contributions. In particular, the excitation of the two-dimensional pattern is obtained at streamwise wavenumbers, where both the first and the second modes synchronize, which confirms the theoretical predictions made by Fedorov[21].

Besides, when only the temperature is considered for the measurement, characteristic scales for P_{2D}, P_O and P_S are well recovered. It suggests that probes limited to the temperature component can be efficient for the velocity fields estimation in the development of control strategies. In addition, when considering both the total energy and kinetic energy contribution for the PSDs associated with the different peaks, increasing the Mach number from low subsonic to supersonic Mach numbers is mainly accompanied with a transfer from kinetic to internal energy with no significant variation of the total energy. A similar conclusion has been made for streaks by[34].

A systematic variation of the wall-normal position, where the forcing is placed, substantially influences the expected response of the boundary layer. While a forcing localized within the δ_{99} boundary layer thickness favours the onset of oblique flow structures, streaks dominate the long time behaviour of stochastically forced supersonic boundary layers as the input is moved away from the wall. If the stochastic input is restricted to only the near-wall region, the spanwise forcing has the biggest impact on the receptivity of both streaks and oblique flow structures for a $M_\infty = 4.5$ case, which is redundant with the behaviour in the incompressible limit[27]. For the amplification of two-dimensional patterns, in contrast, a similar contribution of the wall-normal and streamwise velocity components is observed. To the best of the author's knowledge, the competition between these two different characteristic flow structures has not been elucidated through previous linear receptivity models devoted to supersonic boundary layers. The effect of near-wall temperature excitation is only efficient for the onset of the oblique pattern, which helps to understand the effectiveness in controlling the oblique mode with an actuator based on the temperature.

Finally, to connect the different peaks found in the receptivity coefficient maps to characteristic eddies and their wall-normal structures, the correlation between the velocity and temperature components are emphasized by a comparison between the forcing and response POD modes. On one hand, this study further confirms the efficiency of forcing temperature in triggering the onset of the oblique pattern. On the other hand, it also indicates the wall-normal distribution of the temperature fields for which the stochastic excitation has the strongest impact onto the emergence of the oblique flow structure. Here, the temperature component of the dominant forcing POD mode is mainly concentrated within the δ_{99} boundary layer thickness with a non negligible part near the wall.

The study presented could be extended in several ways. First, the influence of wall heating on

the stochastic receptivity of supersonic boundary layers will provide interesting prospects. Especially, the role of the temperature perturbation onto the different peaks observed in the receptivity coefficients could be greatly altered in comparison with the adiabatic case. Secondly, the investigation of the receptivity coefficient computed with a colored input (*i.e.* with specific space-time correlations aiming to reproduce more realistic external disturbances, see Hœpffner *et al.*[42] for details), is highly desirable and subject of ongoing work. In the same vein, it could be difficult to separately identify the impact of the character of background disturbances in the freestream (either vortical or acoustic). We suggest that the present input/output technique could be extended to overcome this drawback by considering either vorticity components or pressure fields as inputs. Thirdly, the same type of study can be performed in a global framework where the flow direction is taken as an eigendirection to study the receptivity of spatially evolving structures (see Ran *et al.*[26] for the incompressible flow case). This is not straightforward as it requires the computation of a very large covariance matrix which is even more difficult in the compressible regime due to the necessity of using large computational boxes to avoid acoustic reflection[40]. An promising strategy could be to approximate the covariance matrix into a harmonic forcing/response mode basis[43]. For that purpose, a numerical method based on automatic differentiation should be more appropriate to compute then the singular decomposition of the resolvent operator (see Bugeat *et al.*[44]).

5. APPENDIX 1: VALIDATION OF THE LINEAR STABILITY SOLVER

For validation purposes, we report in figure 19(a), neutral curves in (ω_r, Re) plane for the two-dimensional first and second modes (*i.e.* $\beta = 0$), $M_\infty = 4.5$ and $T_0 = 333\ K$. Two grids are considered. The first corresponds to $N = 201,\ y_m = 100$ and the second one is associated with $N = 401,\ y_m = 600$ (*i.e.*, the grid used in the present manuscript). One may observe that there is no significant changes between results obtained by using the first and second grids. The figure 19(a) also shows that results are consistent with computations carried out by Ma & Zhong[16].

Results associated with three-dimensional disturbances are shown in figure 19(b) for the finest grid mesh $N = 401$, $y_m = 600$ for $Re = 300$. Neutral curves for the first and second modes are compared to those extracted from Hanifi *et al.*[10]. One may also observe a good agreement between our curves and those published by the previous authors.

To validate the input/output technique employed in the present manuscript, the incompressible case investigated by Ran *et al.*[26] is carried out by using the same input/output method that the one described in the present manuscript. The incompressible solver is detailed in a previous

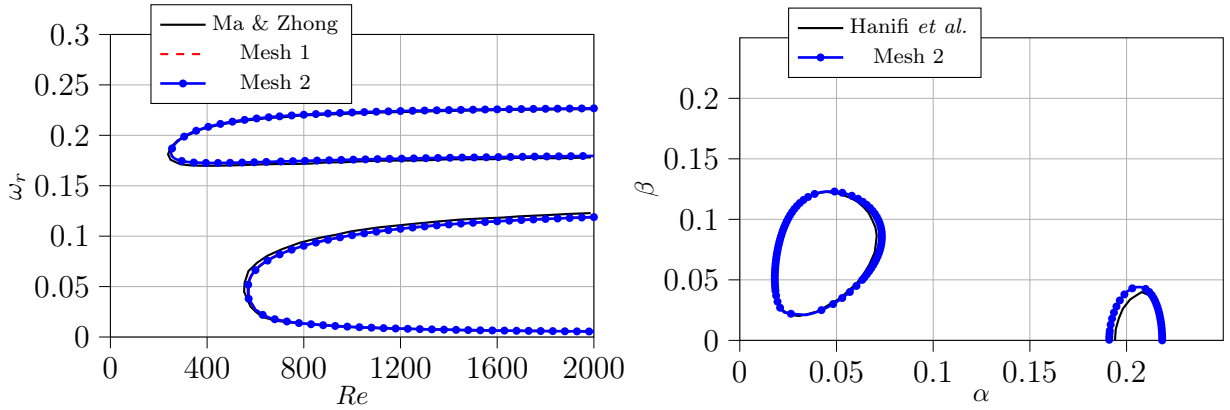

(a) (b)

FIG. 19: Neutral stability curves at $M_\infty = 4.5$ and $T_0 = 333\ K$. (a) Circular frequency, ω_r, vs. Reynolds number Re of two-dimensional first and second modes; In black lines: results extracted from Ma & Zhong[16] are shown. Two grids are considered. Mesh 1: $N = 201$, $y_m = 100$ and Mesh 2: $N = 401$, $y_m = 600$. (b) spanwise wavenumber, β, vs. streamwise wavenumber α of three-dimensional first and second modes at $Re = 300$. In black lines: results extracted from Hanifi *et al.*[10] are shown.

article[45], especially the numerical method to deal with the pressure. The one-dimensional receptivity coefficient computed by integrating $C_R(\alpha, \beta)$ over streamwise wave numbers is shown in figure 20. The figure shows a good agreement with results given by Ran *et al.*[26]. Then, we validate the input/output technique for the compressible case by comparisons between incompressible flow results and low-Mach number flow regime for the same Reynolds number.

Results are displayed in figure 21. The figure shows that receptivity coefficients obtained for the low-Mach number case and the incompressible flow are almost superimposed.

6. APPENDIX 2: LINEAR STABILITY EQUATIONS.

In this appendix, we detail the dimensionless linear stability equations that are used in that manuscript. A continuous formulation is here adopted. The conservation of mass reads:

$$\frac{1}{T}p_t - \frac{1}{T^2}\theta_t + \frac{1}{T}\nabla\cdot\mathbf{u} + v\left(\frac{1}{T}\right)_y + Ui\alpha\left(\frac{1}{T}\Pi - \frac{1}{T^2}\theta\right) = 0.$$

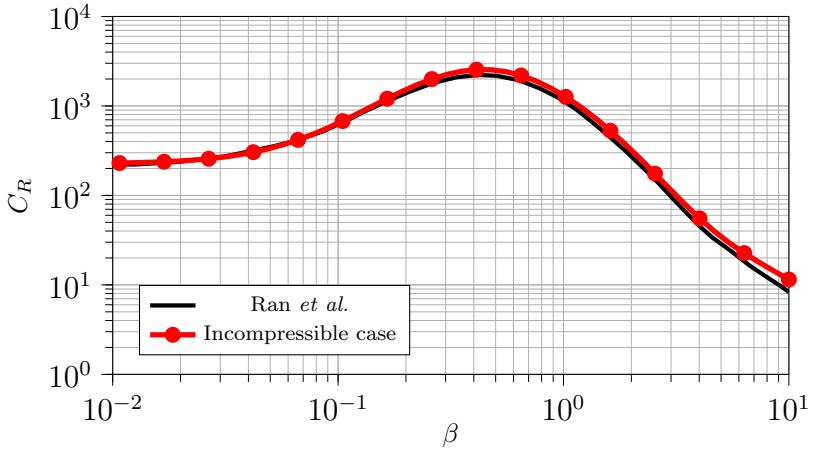

FIG. 20: The one-dimensional receptivity coefficient for the incompressible boundary layer case with $Re = 232$. In full black, results extracted from Ran *et al.*[26] are shown.

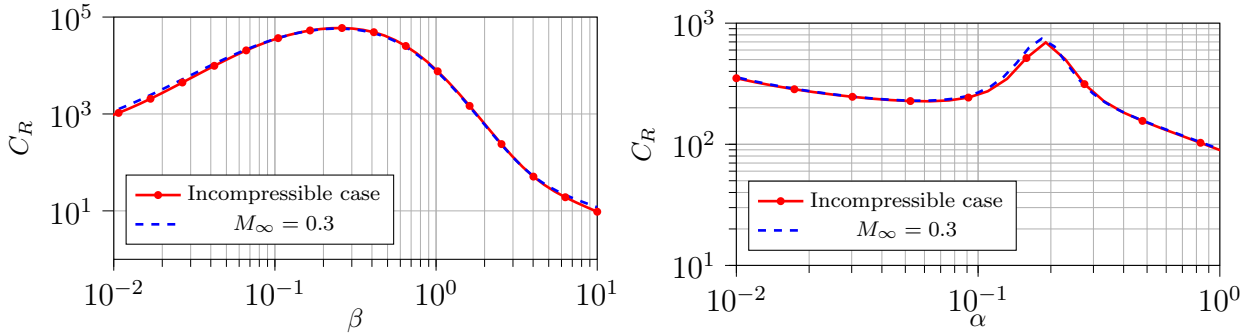

FIG. 21: Receptivity coefficient (a) $C_R(\alpha = 0.0001, \beta)$ and (b) $C_R(\alpha, \beta = 0.01)$ computed for the incompressible case and $M_\infty = 0.3$ for $Re = 232$.

The momentum equation in the x-direction reads:

$$\frac{1}{T}\left(u_t + Uui\alpha + vU_y\right) = -\frac{1}{\gamma M_\infty^2} i\alpha\Pi + \frac{1}{Re}\left[\mu\Delta u + \frac{1}{3}\mu i\alpha\nabla\cdot\mathbf{u} + \mu_T T_y\left(u_y + i\alpha v\right) + \mu_T\left(U_{yy}\theta + U_y\theta_y\right) + \mu_{TT}T_y U_y\theta\right].$$

The momentum equation in the y-direction reads:

$$\frac{1}{T}\left(v_t + Uvi\alpha\right) = -\frac{1}{\gamma M_\infty^2}\Pi_y + \frac{1}{Re}\left[\mu\Delta v + \frac{1}{3}\left(\nabla\cdot\mathbf{u}\right)_y - \frac{2}{3}\mu_T T_y\nabla\cdot\mathbf{u} + 2\mu_T T_y v_y + \mu_T U_y i\alpha\theta\right].$$

The momentum equation in the z-direction reads:

$$\frac{1}{T}\left(w_t + Uwi\alpha\right) = -\frac{1}{\gamma M_\infty^2} i\beta\Pi + \frac{1}{Re}\left[\mu\Delta w + \frac{1}{3}i\beta\nabla\cdot\mathbf{u} + \mu_T T_y\left(w_y + i\beta v\right)\right]$$

The first law of thermodynamics written for the temperature reads:

$$\frac{1}{T}\left(\theta_t + Ui\alpha\theta + vT_y\right) = -\left(\gamma-1\right)\nabla\cdot\mathbf{u} + \frac{\gamma}{PrRe}\left[\mu\Delta\theta + \mu_T T_{yy}\theta + 2\mu_T T_y\theta_y + \mu_{TT}T_y^2\theta\right] + \gamma\left(\gamma-1\right)M_\infty^2\frac{1}{Re}\left[2\mu U_y\left(u_y + i\alpha v\right) + \mu_T\theta U_y^2\right].$$

We note Δ the Laplacian operator:

$$\Delta = -\alpha^2 - \beta^2 + \partial^2/\partial y^2$$

and the divergence operator is

$$\nabla\cdot\mathbf{u} = i\alpha u + v_y + i\beta w.$$

A first order approximation for the fluctuation of $\mu\left(T\right)$ is used :

$$\mu\left(T+\theta\right) - \mu\left(T\right) = \theta\mu_T\left(T\right).$$

---

[1] X. Zhong and X. Wang. Direct numerical simulation on the receptivity, instability, and transition of hypersonic boundary layers. *Ann. Rev. Fluid Mech.*, 44:527–561, 2012.

[2] W.S. Saric, H.L. Reed, and E.J. Kerschen. Boundary-layer receptivity to freestream disturbances. *Ann. Rev. Fluid Mech.*, 34:291–319, 2002.

[3] H.L. Reed, W.S. Saric, and D. Arnal. Linear stability theory applied to boundary layers. *Ann. Rev. Fluid Mech.*, 28:389–428, 1996.

[4] P.J. Schmid. Nonmodal Stability Theory. *Ann. Rev. Fluid Mech.*, 39:129–162, 2007.

[5] L.M. Mack. Special Course on Stability and Transition of Laminar Flows. *AGARD REPORT*, 709, 1984.

[6] D. Arnal. Boundary-layer transition: predictions based on linear theory. *AGARD R*, 793, 1994.

[7] S. Özgen and S. A. Kircali. Linear stability analysis in compressible, flat-plate boundary layers. *Theoret. Comput. Fluid Dynamics*, 22:1–20, 2008.

[8] N. P. Bitter and J. E. Shepherd. Stability of highly cooled hypervelocity boundary layers. *J. Fluid Mech.*, 778:586–620, 2015.

[9] M.T. Landhal. A note on an algebraic instability of inviscid parallel shear flow. *J. Fluid Mech.*, 98: 243–251, 1980.

[10] A. Hanifi, P.J. Schmid, and D.S. Henningson. Transient growth in compressible boundary layer flow. *Phys. Fluids*, 8:826, 1996.

[11] S. Zuccher, A. Tumin, and E. Reshotko. Parabolic approach to optimal perturbations in compressible boundary layers. *J. Fluid Mech.*, 556:189–216, 2006.

[12] A. Tumin and E. Reshotko. Optimal disturbances in compressible boundary layers. *AIAA Journal*, 41: 2357–2363, 2003.

[13] D. Tempelmann, A. Hanifi, and D.S. Henningson. Spatial optimal growth in three-dimensional compressible boundary layers. *J. Fluid Mech.*, 704:251–279, 2012.

[14] D.C. Hill. Adjoint systems and their role in the receptivity problem for boundary layers. *J. Fluid Mech.*, 292:183–204, 1995.

[15] M.R. Malik, R.-S. Lin, and R. Sengupta. Computation of hypersonic boundary-layer response to external disturbances. *37th AIAA*, 11-14 January:A99–16304, 1999.

[16] Y. Ma and X. Zhong. Receptivity of a supersonic boundary layer over a flat plate. part 1. wave structures and interactions. *J. Fluid Mech.*, 488:31–78, 2003.

[17] X. Wang and X. Zhong. Effect of wall perturbations on the receptivity of a hypersonic boundary layer. *Phys. Fluids*, 21:044101, 2009.

[18] A.V. Fedorov and A.P. Khokhlov. Receptivity of hypersonic boundary layer to wall disturbances. *Theoret. Comput. Fluid Dynamics*, 15:231–254, 2002.

[19] A. Tumin, X. Wang, and X. Zhong. Direct numerical simulation and the theory of receptivity in a hypersonic boundary layer. *Phys. Fluids*, 19:014101, 2007.

[20] A. Tumin. Three-dimensional spatial normal modes in compressible boundary layers. *J. Fluid Mech.*, 586:295–322, 2007.

[21] A. Fedorov. Transition and stability of high-speed boundary layers. *Ann. Rev. Fluid Mech.*, 43:79–95, 2011.

[22] B.F. Farrell and P.J. Ioannou. Stochastic forcing of the linearized Navier-Stokes equations. *Phys. Fluids*, 5:2600–2609, 1993.

[23] B. Bamieh and M. Dahleh. Energy amplification in channel flows with stochastic excitation. *Phys. Fluids*, 13:3258–3269, 2001.

[24] P. J. Schmid and D. S. Henningson. *Stability and Transition in Shear Flows*. Applied Mathematical Sciences 142, Springer, 2001.

[25] Y. Hwang and C. Cossu. Amplification of coherent streaks in the turbulent Couette flow: an input-output analysis at low Reynolds number. *J. Fluid Mech.*, 643:333–348, 2010.

[26] W. Ran, A. Zare, M.J.P Hack, and M.R. Jovanović. Stochastic receptivity analysis of boundary layer flow. *Phys. Rev. Fluids*, 4:093901, 2019.

[27] M.-R. Jovanović and B. Bamieh. Componentwise energy of amplification in channel flows. *J. Fluid Mech.*, 534:145–183, 2005.

[28] P. Morra, O. Semeraro, D.S. Henningson, and C. Cossu. On the relevance of Reynolds stresses in resolvent analyses of turbulent wall-bounded flows. *J. Fluid Mech.*, 867:969–984, 2019.

[29] A. Dwivedi, G.S. Sidharth, J.W. Nichols, G.V. Candler, and M.R. Jovanović. Reattachment streaks in hypersonic compression ramp flow: an input-output analysis. *J. Fluid Mech.*, 880:113–135, 2019.

[30] A. Dwivedi, G.S. Sidharth, and M.R. Jovanović. Oblique transition in hypersonic double-wedge flow: an input-output viewpoint. *J. Fluid Mech.*, submitted, 2021.

[31] H.J. Bae, S.T.M. Dawson, and B.J. McKeon. Resolvent-based study of compressibility effects on supersonic turbulent boundary layers. *J. Fluid Mech.*, A29, 2020.

[32] S.T.M. Dawson and B.J. McKeon. Prediction of resolvent mode shapes in supersonic turbulent boundary layers. *Int. J. of Heat and Fluid Flow*, 85:108677, 2020.

[33] F. Alizard, S. Pirozzoli, M. Bernardini, and F. Grasso. Optimal transient growth in compressible turbulent boundary layers. *J. Fluid Mech.*, 770:124–155, 2015.

[34] A. Madhusudanan and B.J. McKeon. Stochastic forcing to a linearized Navier-Stokes based model for laminar compressible boundary layers. *AIAA SciTech 2022 Forum*, 10.2514/6.2022-1370, 2022.

[35] A. Fedorov and A. Tumin. Initial-value problem for hypersonic boundary-layer flows. *AIAA Journal*, 41-3:379–389, 2003.

[36] M.R. Jovanović. From Bypass Transition to Flow Control and Data-Driven Turbulence Modeling: An Input-Output Viewpoint. *Ann. Rev. Fluid Mech.*, 53:311–345, 2021.

[37] B.-T. Chu. On the energy transfer to small disturbances in fluid flow (part i). *Acta Mechanica*, 1:215–234, 1965.

[38] O. Vermeersch. étude et modélisation du phénomène de croissance transitoire pour des couches limites incompressibles et compressibles. *Doctoral thesis. Supaero ISAE.*, 2009.

[39] C. Tam and Z. Dong. Radiation and outflow boundary conditions for direct computation of acoustic and flow disturbances in a nonuniform mean flow. *J. Comput. Acoustics*, 4:175–201, 1996.

[40] O. Kamal, G. Rigas, M.T. Lakebrink, and T. Colonius. Application of the One-Way Navier-Stokes (OWNS) equations to hypersonic boundary layers. *AIAA AVIATION 2020 FORUM*, 10.2514/6.2020-2986, 2020.

[41] A. Fedorov and A. Tumin. High-speed boundary-layer instability: Old terminology and a new framework. *AIAA Journal*, 49:1647–1657, 2011.

[42] J. Hœpffner, M. Chevalier, T.R. Bewley, and D.S. Henningson. State estimation in wall-bounded flow systems. part 1. perturbed laminar flows. *J. Fluid Mech.*, 534:263–294, 2005.

[43] G. Dergham, D. Sipp, and J.-C. Robinet. Stochastic dynamics and model reduction of amplifier flows: the backward facing step flow. *J. Fluid Mech.*, 719:406–430, 2013.

[44] B. Bugeat, J.-C. Chassaing, J.-C. Robinet, and P. Sagaut. 3D global optimal forcing and response of the supersonic boundary layer. *J. Computational Physics*, 398:108888, 2019.

[45] S. Lebbal, F. Alizard, and B. Pier. Revisiting the linear instabilities of plane channel flow between compliant walls. *Physical Review Fluids*, 7:023903, 2022.